Structural changes in borosilicate glasses as a function of Fe2O3 content: A multi-technique approach

EALES, J.D. <http://orcid.org/0000-0001-6914-0341>, BELL, A.M.T., CUTFORTH, D.A., KRUGER, A.A. and BINGHAM, Paul <http://orcid.org/0000-0001-6017-0798>

Published version

EALES, J.D., BELL, A.M.T., CUTFORTH, D.A., KRUGER, A.A. and BINGHAM, Paul (2023). Structural changes in borosilicate glasses as a function of Fe2O3 content: A multi-technique approach. Journal of Non-Crystalline Solids, 622: 122664.

Journal of Non-Crystalline Solids 622 (2023) 122664

Contents lists available at ScienceDirect

Journal of Non-Crystalline Solids

journal homepage: www.elsevier.com/locate/jnoncrysol

Structural changes in borosilicate glasses as a function of Fe_2O_3 content: A multi-technique approach

J.D. Eales [a,*], A.M.T. Bell [a], D.A. Cutforth [b], A.A. Kruger [c], P.A. Bingham [a,*]

[a] Materials and Engineering Research Institute, Sheffield Hallam University, Sheffield, S1 1WB, UK
[b] Pacific Northwest National Laboratory, Richland, WA 99352, USA
[c] U.S. Department of Energy, Office of River Protection, Richland, WA, USA

ARTICLE INFO

Keywords:
Radioactive waste glass
Borosilicate glass
Iron oxide
Mössbauer spectroscopy
X-ray absorption – near edge structure spectroscopy
X-ray photoelectron spectroscopy

ABSTRACT

Three series of borosilicate glasses were prepared, ranging from simple ternary sodium borosilicate glasses (SCFe series), to complex borosilicate glasses (CCFe Series), to high-level radioactive waste analogue glasses (HAFe series). ^{57}Fe Mössbauer and Fe K-edge XANES spectroscopies showed that the iron exists exclusively as Fe^{3+} in predominantly distorted tetrahedral structures ($^{[4]}Fe^{3+}$), with evidence for lower abundances of higher-coordinated $^{[5\ or\ 6]}Fe^{3+}$. Raman, B K-edge XANES, and XPS spectroscopies qualitatively demonstrated that Fe^{3+} preferentially integrates into the borosilicate network through the silicate sub-network in the simple glasses, whereas in the complex glasses it preferentially integrates through the borate sub-network. The $^{[4]}B^{3+}$ fraction for the SCFe and CCFe glasses showed minimal changes as a function of Fe content, indicating that Fe concentration has no effect on boron coordination and is- therefore unlikely to be competing with $^{[4]}B^{3+}$ groups for charge compensation, qualitatively supporting the presence of competing tetrahedral avoidance hierarchies.

1. Introduction

The Hanford site in Washington State, USA, is host to approximately 200,000 m^3 of mixed hazardous waste, historically stored in 177 tanks from 45 years of plutonium production that started in 1944 as part of the "Manhattan Project". The plutonium was produced in uranium fission reactors, with the plutonium being extracted in reprocessing plants before it was then sent to another site to be further processed into nuclear weapons [1]. The reprocessing plants utilised several distinct extraction processes, including the "Bismuth Phosphate", "REDOX" (Reduction and Oxidation) process, and the "PUREX" (Plutonium and Uranium Extraction) processes, that contributed to the generation of the complex nuclear wastes [1–3]. These processes utilised various Fe-bearing compounds, such as ferrous sulphamate, and nickel ferrocyanide, which resulted in large quantities of iron-bearing waste being formed [2,3]. To immobilise the radionuclides present in these tank wastes, they will be vitrified into borosilicate glass using a "direct feed" approach at the Waste Treatment and Immobilization Plants (WTPs) now under construction and becoming operational at the Hanford site [4]. The final waste-forms will be highly complex, with each component having a unique effect on the resulting vitrified product structure and properties.

Iron has long been used in commercial glass manufacture as a colouring agent [5,6] and has also been used to improve the processability of glass [7]. Iron within oxide glasses acts as a glass network intermediate, i.e.it can both polymerise and depolymerise the glass network and consequentially, will influence the glass properties in different ways [8–10]. Iron exists as multivalent and multi-coordinated species within oxide glasses, with the preferential valency and structure being dependent on a variety of factors such as the batch and glass compositions, melting atmosphere and environment, and abundance of Fe [11]. This makes it incredibly challenging to predict how the iron will exist within a given glass and how it will influence the glass properties. Many studies have elucidated some of the nature of iron within glass across a variety of glass matrices, including phosphate (see, for example, [12–14]), silicate (see, for example, [8,9,15-17]), and borosilicate glasses (see, for example, [18–20]). Within phosphate glasses, it is found that the addition of Fe_2O_3 increases the chemical durability where the concentration of Fe^{2+}/Fe_{Total} increased with melting temperature [13]. The chemical durability was not affected by the changing melt times as both the Fe^{3+} and Fe^{2+} existed in 6-coordinated sites, so both were able to form the more chemically-durable Fe-O-P bonds relative to the P-O-P bonds they replace [13,14]. Within silicate glasses, without the use of a reducing or oxidising agent during melting, the majority of the iron exists as

* Corresponding authors.
E-mail addresses: james.eales@student.shu.ac.uk (J.D. Eales), p.a.bingham@shu.ac.uk (P.A. Bingham).

https://doi.org/10.1016/j.jnoncrysol.2023.122664
Received 28 April 2023; Received in revised form 14 August 2023; Accepted 27 September 2023
Available online 4 October 2023

charge-compensated tetrahedral Fe^{3+} ($^{[4]}Fe^{3+}$), integrating within the silicate network as network formers, with network modifying Fe^{3+} and Fe^{2+} six-coordinated structures [15–17]. Bingham et al. [17] used Fe K-edge EXAFS to elucidate the nature of the structure of dilute Fe^{3+} in silicate glasses and found that alkali and alkaline earth modifiers had a significant effect on the average coordination of Fe^{3+}, with alkali metal modifiers being more likely to stabilise $^{[4]}Fe^{3+}$units. Studies of borosilicate glasses showed that a considerable amount of iron exists as $^{[4]}Fe^{3+}$ that can integrate within the tetrahedral borosilicate network, alongside the presence of six coordinated Fe^{3+} and Fe^{2+}, both of which modify the borosilicate network [18,20]. Wright et al. [19] reported that the $^{[4]}Fe^{3+}$ in a simple sodium borosilicate glass will likely preferentially integrate within the silicate sub-network rather than the borate sub-network, based on the existence (or lack thereof in some cases) of analogous crystalline materials, coupled with neutron diffraction data.

Within the context of nuclear waste glasses, there has been considerable research into how Fe influences secondary phase stabilisation, particularly in US waste glasses which can have high Fe contents. Specific research interests include the links between transition metals and secondary crystalline phases such as spinel crystals and nepheline. The interests in spinel crystals are primarily due to the risk spinel phases pose to glass melters (see, for example, [21–23]). Spinel crystals can accumulate within the melter systems, particularly in the pouring spouts, as a result of the temperature decrease from the furnace chamber to the pouring spout [22], which can result in clogging and obstruction of the pouring spout. This can lead to significant shortening of melter lifetimes if not adequately accounted for. Nepheline crystals provide a different set of problems by reducing the chemical durability of the final waste form by removing alumina and silica from the glass (see, for example, [24–26]). Ahmadzadeh et al. [25] studied nepheline-based glasses and the role of iron in the formation of nepheline by substituting the Al_2O_3 for Fe_2O_3. It was found that at low Fe abundances, $^{[4]}Fe^{3+}$ could substitute into as much as 37 % of the $^{[4]}Al^{3+}$ sites, however, at higher abundances, Fe would preferentially form magnetite or haematite phases. Jantzen & Brown [21] found that the octahedral site preference energy (OSPE) order for the formation of spinel crystals in complex nuclear waste glasses is $Ni^{2+} \approx Fe^{2+} > Mg^{2+} > Mn^{2+}$. Further work by Jantzen & Brown [24] showed that waste glasses with less than 50 wt. % SiO_2 may also result in nepheline crystallisation with the potential for $^{[4]}Fe^{3+}$ occupying a site in the nepheline structure. With the variety of oxidation states and coordination numbers Fe can assume in glasses, and the numerous factors that can influence Fe chemistry, better understanding of how Fe integrates into complex glasses is required so that effects on the Hanford-specific radioactive waste forms can be more accurately predicted. Furthermore, chemical durability is a key property of vitrified radioactive waste, with iron chemistry being linked to chemical durability in borosilicate simulant waste glasses [27]. Cassingham et al. [27] demonstrated that tetrahedral Fe^{3+} can have a non-linear positive influence on chemical durability, this study was done in respects to iron-only. Numerous studies, for example those summarised in [28], have shown that iron has mixed impact on chemical durability of radioactive waste borosilicate glasses, when compared to the effects of other cations within the glass. For example, when Fe is substituted for Al or Zn, the glass durability increases with respects to normalised leach rates of the key glass components [29,30]. Understanding the chemistry of the iron within radioactive waste glasses, will allow for an increased level of predictability in how the Fe may impact chemical durability of the self-same waste glasses.

This research has utilised a multi-spectroscopic approach, similar to studies by Cochain et al. [18] and Ciżman et al. [20] to consider three borosilicate glass families with increasing chemical (and consequently structural) complexity, from simple sodium borosilicate glasses to inactive high-Fe Hanford analogue glass composition derived from the HLW-Ng-Fe2 waste composition [31]. Iron chemistry has been characterised by Mössbauer and Fe K-edge X-ray absorption – near edge structure (XANES) spectroscopies, while Raman and X-ray photoelectron (XPS) spectroscopies have been used to provide complementary structural information. Boron K-edge XANES has been used to characterise boron coordination as a function of base glass composition and Fe content, as there is a reported link between Fe and B speciations (albeit with no consensus yet on the nature of this link) [18,26,32]. The combined analyses performed will help to provide a more complete understanding of the structural impacts of Fe on glasses directly relevant to radioactive waste immobilisation.

2. Experimental procedures

2.1. Samples and sample preparation

Three series of borosilicate glasses were designed for this study, with all three starting with an iron-free base glass, which is then incrementally doped in a pro-rata basis with Fe_2O_3. The first series is a simple sodium borosilicate glass with only 3–4 components in the series (Table 2). The data was derived from a compilation of non-active waste simulants provided by the Pacific Northwest National Laboratory (PNNL). A sodium borosilicate glass was selected due this particular matrix being the simplest compositional starting point without changing the fundamental glass matrix (to either a borate or silicate glass). The exact composition was taken from averaging the high-level radioactive waste (HLW) glass compositional data provided, and was then simplified using the following rules:

1) SiO_2 and B_2O_3 contents were kept the same.
2) All group 1 and 2 oxides were represented on a mole-for-mole basis by Na_2O.
3) All other components were removed, and the remaining composition was normalised to 100 %.

To supplement this decision, there is significant established literature on Fe-doped sodium borosilicate glasses (see for example [18–20]) with which to compare the results from this study. Though care is taken when comparing the results in this research to those by Cizman et al. [20] as the borosilicate glasses in this research do not fall within the phase separation region of a ternary borosilicate system, whereas the glasses studied by Cizman et al. [20] do fall within this region. This is due to Cizman et al. [20] studying the influence iron has on the electronic conductivity in porous, phase separated NBS (Na-borosilicate) glasses. Therefor any comparisons between this study and Cizman et al. [20] will be made with careful considerations of the differences in composition and research focus.

The second series is a more complex borosilicate glass with lithium, calcium, and aluminium oxides included in the composition (Table 3). These additional components are commonly found across a variety of glasses, as well as being present within a lot of the expected Hanford waste glasses. This series aims to introduce more compositional complexity, while also making sure it is comparable to wider literature [33–38]. The rules that lead to the derivation of this composition, starting with the same average composition that provided the sodium borosilicate glass, are as followed:

1) SiO_2, B_2O_3, Al_2O_3 and Li_2O contents were kept the same.
2) All group 1 oxides were represented on a mole-for-mole basis by Na_2O.
3) All group 2 oxides were represented on a mole-for-mole basis by CaO.
4) All other components were removed, and the remaining composition was normalised to 100 %.

The third series is derived from the HLW Ng-Fe2 Hanford simulant waste glass composition studied by Rodriguez et al. [31] (Tables 4a and 4b). The HLW Ng-Fe2 was selected as high-Fe waste simulant with basic characterisation and property data available for comparison [31,39,40].

Oxide components that had an abundance of less than 0.05 wt % were excluded with the exception of zinc oxide (ZnO),as zinc oxide has a unique effect on the glass matrix, even in low abundances [41].

Series 1 is referred to as the SCFe series (Simplified Composition – Fe-doped series), Series 2 is referred to as the CCFe series (Complex Composition – Fe-doped series), and Series 3 is referred to as the HAFe series (Hanford Analogue – Fe-doped series).

The samples were prepared by batching and mixing powdered raw materials (see Table 1 for details of the raw materials), using a KERN PCB precision balance with an accuracy of ± 0.005 g. All but the boric acid (H_3BO_3), diammonium phosphate ($(NH_4)_2HPO_4$), lead oxide (PbO), lanthanum hydroxide ($La(OH)_3$), and zirconium hydroxide ($Zr(OH)_4$), were dried for at least 24 hrs prior to batching at 110 °C. The diammonium phosphate and lead oxide could not be dried due to COSHH (Control Of Substances Hazardous to Health) constraints. The boric acid loses bonded water below 100 °C, therefor did not need to be specifically dried. The batches were designed to produce a theoretical yield of 75 g of glass, resulting in batches that ranged from approximately 80–100 g in mass, depending on exact composition. Each batch was stored for no longer than 18 h in ambient conditions before being melted. The batch was mixed by tumbling the batched raw materials in a bag until the colour of the combined batch is homogenised by eye. The mixed batch was then loaded into a Pt/Rh crucible into a furnace pre-heated to 1150 °C. The crucible remained static in the furnace for 1 h, before being removed from the furnace and the glass poured and quenched onto a cast-iron quench plate. The quenched glass was then milled in a tungsten carbide rotational mill before being loaded back into the Pt/Rh crucible and melted for an additional hour, before being poured into pre-heated cast iron moulds and annealed in an electric furnace at 475 °C for 1 h then cooled slowly to room temperature. This method of melting-milling-melting was employed to increase sample homogeneity.

With the exception of the annealing temperatures and times, the methods used to generate the samples are closely linked to those employed within the wider body of research on Hanford waste glasses (see for example [31,39,40]). The melting temperature was selected to be the expected operating temperatures of the melters at the Hanford WVP [39,40]. The annealing temperature was selected based on preliminary sodium borosilicate glass samples that exhibited neither secondary phase formation nor sample cracking after being annealed at 475 °C.

2.2. Compositional analysis

2.2.1. X-ray fluorescence (XRF) spectroscopy

For X-ray fluorescence (XRF) spectroscopy measurements, samples were prepared by mixing ~1 g of glass powder with ~10 g of lithium tetraborate ($Li_2B_2O_7$) flux doped with 0.5 % lithium iodide (LiI) anti-cracking agent. The mixture was melted in a platinum crucible in a LeNeo automatic fusion system at 1065 °C for 21 min and 45 s, then poured and cooled, forming a homogenous fused bead. The samples were analysed by Glass Technology Services using a version of the Glass OXI program [42]. The uncertainty on the measured values was quoted as ± 2 % relative to value given.

Table 1
Raw materials used to produce batches for all glasses.

Target oxide	Raw material (Purity)[a]	Target oxide	Raw material (Purity)[a]	Target oxide	Raw material (Purity)[a]
Al_2O_3	$Al(OH)_3$ (LR)	Li_2O	Li_2CO_3 (99 %)	SO_3	Na_2SO_4 (> 99 %)
B_2O_3	H_3BO_3 (99.99 %)	MgO	$MgCO_3$ (LR)	SiO_2	Purified sand (LR)
CaO	$CaCO_3$ (LR)	MnO_2	MnO_2 (≥ 99 %)	SrO	$SrCO_3$ (LR)
CeO_2	CeO_2 (99.9 %)	Na_2O	Na_2CO_3 (LR)	ZnO	ZnO (≥ 99 %)
Cr_2O_3	Cr_2O_3 (98+%)	NiO	NiO (99.99 %)	ZrO	$Zr(OH)_4$ (> 97 %)
Fe_2O_3	Fe_2O_3 (≥ 96 %)	P_2O_5	$(NH_4)_2HPO_4$ (≥ 98 %)		
La_2O_3	$La(OH)_3$ (99.95 %)	PbO	PbO (LR)		

[a] Purity values provided by suppliers. "LR" means "Lab/Reagent Grade" - Actual purity values of these chemicals were not stated.

2.2.2. ICP-MS

Inductively Coupled Plasma – Mass Spectroscopy (ICP-MS) was used to determine the elemental abundance of boron and lithium within the samples, as these elements are too light to be detected by the XRF available. Powdered samples weighing 500 ± 1 mg were added to an acid solution ($4HNO_3 + 3HF + 2HCl + 2H_2O$) and extracted using an Anton Paar microwave digestion system. After digestion, 2 trials of the sample were diluted to 50 ml with a third trial spiked with a known quantity of Li (in applicable samples only) and B. The third sample was used to calculate the recovery factor. All trials were measured using a Perkin Elmer Nexion-1000 ICP - Mass Spectrometer with a calibration method. The recovery factor was applied to refine the measurement after subtracting the acid blanks. The uncertainties of the measurements were quoted as ± 2.7 % of the measured values for boron, and ± 3.8 % of the measured values for lithium. The elemental weight percentages were converted oxide weight percent values on the assumption that 100 % of the lithium exists as Li_2O within the samples, and 100 % of the boron exists as B_2O_3 within the samples. These values where used in combination with the oxide weight percent values from the XRF analyses to generate analysed oxide molar percent compositions for all samples based on the combination of ICP-MS and XRF analyses. The final uncertainties for each value were calculated using the given uncertainty ranges and for the two analysis techniques and propagated using the partial derivative method. These values can be seen in Tables 2,3 and 4b.

2.2.3. Density

Glass density was measured and calculated in accordance with Archimedes' principle detailed by Eq. (1) below.

$$\rho_m = \frac{m_{air}}{m_{air} - m_{water}}\rho_w \quad (1)$$

Where ρ_m is the density of the sample, ρ_w is the temperature dependent density of water, m_{air} is the mass in open air, and m_{water} is the object mass submerged in water. The masses were measured using a KERN YBD-03 precision balance. 400 ml of deionised water was used. The temperature of the water was 20 °C, measured using a mercury-in-glass thermometer, which corresponded to $\rho_w = 0.998203$ g cm^{-3}. For each sample, three separate fragments of glass were measured, and the corresponding densities were averaged with an associated standard error generated.

2.2.4. X-ray diffraction

Approximately 0.5 g of each powdered sample, placed on flat plate sample holders, was loaded into a Panalytical X'Pert Pro-X-ray powder diffractometer. Diffraction patterns were collected using a Cu anode X-ray tube at 40 mA/40 kV power. A mask of 20 mm was used, with the angle range set at 5–50 ° 2θ, at an increment of 0.013 ° 2θ with 97.92 s per step. The stage used was a spinner stage, at 4 revolutions per second to minimise any sample texture effects. Peak identification was carried out using PANalytical Highscore plus software with the International Centre for Diffraction Data (ICDD) database.

2.3. Structural analysis

2.3.1. ^{57}Fe Mössbauer spectroscopy

^{57}Fe Mössbauer spectra for all samples with at least 5 mol % Fe_2O_3

Table 2
Nominal and analysed oxide compositions of the SCFe series samples.

Sample ID	Oxide composition (mol %)							
	SiO_2		B_2O_3		Na_2O		Fe_2O_3	
	Nominal	Analysed[a]	Nominal	Analysed[a]	Nominal	Analysed[a]	Nominal	Analysed[a]
SCFe000.0	55.81	56.88 (± 3.01)	16.28	16.53 (± 1.18)	27.91	26.60 (± 1.41)	0.00	0.00 (± 0.00)
SCFe000.1	55.76	56.85 (± 3.07)	16.26	16.28[b]	27.88	26.67 (± 1.44)	0.10	0.19 (± 0.01)
SCFe000.2	55.70	56.72 (± 3.04)	16.25	16.27[b]	27.85	26.72 (± 1.43)	0.20	0.29 (± 0.02)
SCFe000.5	55.53	56.80 (± 3.17)	16.20	16.22[b]	27.77	26.37 (± 1.47)	0.50	0.61 (± 0.03)
SCFe001.0	55.26	54.93 (± 1.56)	16.12	16.32 (± 0.62)	27.63	27.69 (± 0.79)	1.00	1.06 (± 0.03)
SCFe002.0	54.70	54.80 (± 1.51)	15.95	15.96[b]	27.35	27.21 (± 0.75)	2.00	2.03 (± 0.06)
SCFe003.0	54.14	54.18 (± 1.43)	15.79	16.01 (± 0.54)	27.07	26.72 (± 0.70)	3.00	3.09 (± 0.08)
SCFe004.0	53.58	53.89 (± 1.39)	15.63	15.64[b]	26.79	26.41 (± 0.68)	4.00	4.06 (± 0.10)
SCFe005.0	53.02	52.78 (± 1.38)	15.47	16.21 (± 0.57)	26.51	25.88 (± 0.68)	5.00	5.14 (± 0.13)
SCFe007.5	51.63	51.58 (± 1.36)	15.06	15.62 (± 0.53)	25.81	25.19 (± 0.66)	7.50	7.61 (± 0.20)
SCFe010.0	50.23	50.04 (± 1.28)	14.65	15.47 (± 0.54)	25.12	24.38 (± 0.63)	10.00	10.10 (± 0.26)
SCFe014.0	48.00	48.59 (± 1.25)	14.00	14.02[b]	24.00	23.28 (±0.60)	14.00	14.11 (± 0.36)

[a] B_2O_3 analysed using ICP-MS, everything else analysed using XRF.
[b] Nominal values used in calculating normalised mol %.

were measured using a ^{57}Co gamma source. All spectra were measured at room temperature with a velocity range +/- 4 mm s^{-1} with the exception of HAFe007.3 and HAFe010.0, which were measured at +/- 12 mm s^{-1}. The samples were loaded into acrylic sample disks with an area of 1.767 cm^2. Gamma rays of 14.4 keV were supplied by the cascade decay of 25 mCi ^{57}Co in a rhodium matrix source oscillated at a constant acceleration by a SeeCo W304 drive unit. The detector is a SeeCo 45,431 Kr proportional counter operating with a bias voltage of 1.720 kV applied to the cathode. All measurements were calibrated relative to alpha-Fe foil, with all spectral data fitted using the Recoil software package [43], using Lorentzian line shapes. It was assumed here that the recoil-free fraction ratio, $f(Fe^{3+}/Fe^{2+}) = 1.0$, for any estimation of redox ratios obtained from the fitted spectra although no measurable levels of Fe^{2+} were observed in the studied glasses. We note that it has been suggested that the proportion of Fe^{3+} can be slightly increased relative to Fe^{2+} due to a larger recoil-free fraction, rendering Fe^{3+}/Fe^{2+} ratios for glasses obtained from Mössbauer spectroscopy fitted area ratios, in some cases, higher than actual values [11].

2.3.2. Fe K-edge XANES

Iron K-edge XANES was acquired using the XMaS BM28 beamline at the ESRF in Grenoble, France via remote access during the Covid lockdown period. Pressed pellets of 13 mm diameter were made by pressing 50 mg of a mix of sample powder with cellulose acetate flux. The sample percentage range for each pellet ranged from ~10 – ~50 %, depending on the iron content within the sample (lower iron content required more sample in the mix and vice versa). The spectra were acquired at the Fe K-edge (approximately 7112 eV), by collecting data over a photon energy range of 7000–8200 eV to give a *k*-range up to approximately 15. The spectra were collected with an energy step of 0.1 eV from 100 eV prior to the Fe K-edge, to 200 eV past the edge for the SCFe and CCFe series samples, but a larger step size of0.2 eV was used by the operators to measure the HAFe series samples. For the remainder of the energy range, an energy step size of 0.5 eV was used. Using measured mineral standards haematite (Fe_2O_3), aegirine ($NaFeSi_2O_6$), and staurolite ($Fe_2Al_9O_6(SiO_4)_4(O,OH)_2$), a correction for the Si ⟨111⟩ monochromator angle drift was calculated using Eq. (2) [44]:

$$E_{corrected} = \frac{Eg}{\sqrt{E^2 - g^2}\sin(\Delta\theta) + g\cos(\Delta\theta)} \quad (2)$$

Where $E_{corrected}$ is the corrected energy value, E is the detected energy of the photon, g is an energy constant for the Si 111 monochromator of 1977.1 eV [40], and $\Delta\theta$ is the angle drift. Data were normalised using ATHENA software [45].

2.3.3. B K-edge XANES

Boron K-edge XANES spectra were acquired at the BEAR beamline [46] at the Elettra synchrotron in Trieste, Italy. Pressed pellets of 13 mm diameter were made from mixing 20 mg of sample powder to 180 mg of cellulose acetate flux. The spectra were acquired around the boron K-edge (approximately 194 eV), with a photon energy range of 170–220 eV with an energy step of 0.1 eV. The measurements were performed in fluorescence mode, with the Si K-edge and C K-edge used to create a first-order energy calibration polynomial. Measurements were performed under vacuum conditions due to the X-rays being low energy. For each sample, repeat measurements were performed to improve signal-to-noise statistics for each sample spectrum.

The boron K-edge XANES data was first processed to calculate the μx values for each energy. This was performed using Eq. (3):

$$ln\frac{I}{I_0} = -\mu x \quad (3)$$

Where I is the measured intensity after the sample and I_0 is the measured intensity before the sample. The subsequently data was then normalised in the ATHENA software [42], before being analysed using Origin Pro-software.

2.3.4. Raman spectroscopy

Raman spectra were generated using a Thermo Fisher DX2 Raman spectrometer. Measurements were performed using a 532 nm laser at 10 mW power, with a 600 lines mm^{-1} monochromator across a Raman shift range of 50–3800 cm^{-1}, with a 50 μm slit, and 10x zoom aperture. The samples were in bulk form, with the measured surface being polished flat using SiC paper from P100 grit to P600 grit. The spectra were initially processed using Omnic software, where a proprietary "polynomial 5″ fluorescence correction was applied to all spectra, as all spectra showed signs of fluorescence. From there, the Neuville and Mysen version [47] of the Long correction (Eq. (4)) [48] was applied to all spectra.

$$I = I_{obs} \cdot \left[\nu_0^3\left[1 - exp(-hc\nu / kT)\right]\nu / (\nu_0 - \nu)^4\right] \quad (4)$$

Where, h is Planck's constant, k is the Boltzmann constant, c is the speed of light, T is the absolute temperature, ν_0 is the wavenumber of the incident laser light and ν is the measured Raman shift. The corrected data was then baseline corrected and normalised using vector normalisation (Eq. (5)) [49].

$$x_{norm} = \frac{x_i}{\sqrt{\sum x_i^2}} \quad (5)$$

This normalisation method was chosen over the more commonly

Table 3
Nominal and analysed oxide compositions of the CCFe series samples.

Sample ID	Oxide composition (mol %)											
	SiO_2		B_2O_3		Na_2O		CaO		Li_2O		Al_2O_3		Fe_2O_3	
	Nominal	Analysed[a]	Nominal	Analysed[a]	Nominal	Analysed[a]	Nominal	Analysed[a]	Nominal	Analysed[a]	Nominal	Analysed[a]	Nominal	Analysed[a]
CCFe000.0	44.12	46.18 (± 1.12)	12.84	13.02 (± 0.43)	22.01	23.26 (± 0.56)	5.36	5.32 (± 0.13)	8.23	4.74 (± 0.22)	7.45	7.48 (± 0.18)	0.00	0.00 (± 0.00)
CCFe001.0	43.68	44.57 (± 1.08)	12.71	13.52 (± 0.44)	21.79	22.49 (± 0.54)	5.30	5.50 (± 0.13)	8.15	5.37 (± 0.25)	7.37	7.37 (± 0.18)	1.00	1.19 (± 0.03)
CCFe003.0	42.79	47.11 (± 1.14)	12.45	8.69 (± 0.28)	21.35	23.65 (± 0.57)	5.20	5.88 (± 0.14)	7.99	3.55 (± 0.16)	7.22	7.72 (± 0.19)	3.00	3.39 (± 0.08)
CCFe005.0	41.91	44.03 (± 1.01)	12.20	12.68 (± 0.39)	20.91	21.24 (± 0.49)	5.09	5.26 (± 0.12)	7.82	4.57 (± 0.20)	7.07	7.11 (± 0.16)	5.00	5.12 (± 0.12)
CCFe007.5	40.81	42.03 (± 1.05)	11.86	12.05 (± 0.41)	20.36	20.86 (± 0.52)	4.96	5.14 (± 0.13)	7.62	5.14 (± 0.24)	6.89	6.93 (± 0.17)	7.50	7.86 (± 0.20)
CCFe010.0	39.71	42.91 (± 1.00)	11.55	11.79(± 0.37)	19.81	19.77 (± 0.46)	4.82	4.84 (± 0.11)	7.41	3.49 (± 0.16)	6.70	6.89 (± 0.16)	10.00	10.30 (± 0.24)

[a] Lithium and Boron were analysed using ICP-MS, the rest were analysed using XRF.

used min-max normalisation method, due to the apparent shift in the maximum point as each and all three series progress (see Figs. 17–19 for an illustration of this). While typically not an issue for peak fitting, it is an issue when assessing the relative changes in Raman band intensity through a series of samples. The vector normalisation technique solves this problem by normalising the spectrum in the x-plane instead of the y-plane [49] (see Figs. S1–S10 in the supplementary material for a visual comparison between the vector normalisation and min-max normalisation).

2.4. X-ray photoelectron spectroscopy

A Kratos Ultra Hybrid spectrometer with a monochromated Al K-alpha X-ray source (1486.6 eV) was used to collect spectra. The samples were loaded onto a sample holder, and then placed into a vacuum chamber. The samples were then transferred to the measurement chamber where each sample was aligned. The alignment was performed by positioning the sample such that the Oxygen 1 s peak (selected for being the most abundant element in the sample) generated a high-count rate (> 5000 per min). For the first five samples, a survey scan using a single sweep of 80 eV pass energy, and a dwell time of 500 ms was used across the full energy range of the instrument. This allowed target energy ranges for specific elements to be set and programmed for scanning. The energy ranges are detailed in Table 5.

For the targeted regions, the pass energy was lowered to 20 eV, the number of sweeps was increased depending on the signal (see Table 5), and the dwell time was increased to 1000 ms. This was all carried out to generate the highest quality spectra for each element. Each signal was then grouped by sample and prepared for data processing. The data was processed using CasaXPS to calibrate the spectra for monochromator drift using the opportunistic C 1 s signal from environmental carbon sources, with further analysis done using OriginPro software.

3. Results

3.1. Compositional analysis & density

The analysed compositions shown in Tables 2,3,4a, and 4b are all broadly comparable to the nominal values intended for each composition with few exceptions. One notable exception can be seen in Table 3, where the analysed B_2O_3 and Li_2O_3 concentrations are significantly lower than the corresponding nominal concentrations in the CCFe003.0 sample. Table 4b shows several low-abundance oxides such as CeO_2 and La_2O_3 were not detectable in the sample, this is attributed to the detection limits of the XRF spectrophotometer, and it is assumed that these oxides are present in the sample as expected.

Within each of the three series of glass samples, the density increases as the Fe_2O_3 contents increase (see Table 6). This can be explained by considering the fact that iron is a relatively heavy element when compared to the major components of the glass (i.e. Si and B), it will increase the density assuming it is incorporated into the glass network.

3.2. X-ray diffraction

The XRD patterns showed no discernible secondary crystalline phases within the glasses from the SCFe and CCFe series, with data for both series showing the characteristic diffuse X-ray scattering pattern between approximately 15.0 and 37.5 ^{o} 2θ, characteristic of silicate glass and amorphous materials (Figs. 1 and 2). The same diffraction pattern was also observed for the HAFe series samples, however, samples HAFe007.1 and HAFe010.0 also showed the presence of a secondary crystalline phase within the glass (Fig. 3).

The HighScore plus software identified this peak pattern as likely being a mixed transition metal oxide spinel phase, which is a common crystalline phase seen in high-Fe Hanford glasses [21-23,39,40]. The intensity of the detected peaks increases as the iron oxide content

Table 4a
Nominal oxide compositions of the HAFe series samples.

Sample ID	Nominal oxide composition (mol %)																		
	Al_2O_3	B_2O_3	CaO	CeO_2	Cr_2O_3	Fe_2O_3	La_2O_3	Li_2O	MgO	MnO_2	Na_2O	NiO	P_2O_5	PbO	SO_3	SiO_2	SrO	ZnO	ZrO_2
HAFe000.0	4.25	15.35	0.72	0.05	0.12	0.00	0.01	4.03	0.31	3.53	16.59	0.49	0.35	0.22	0.21	52.89	0.15	0.03	0.71
HAFe001.0	4.20	15.20	0.71	0.05	0.12	1.00	0.01	3.99	0.31	3.49	16.42	0.48	0.35	0.22	0.21	52.36	0.14	0.03	0.70
HAFe003.0	4.12	14.89	0.70	0.05	0.12	3.00	0.01	3.91	0.30	3.42	16.09	0.47	0.34	0.21	0.20	51.30	0.14	0.03	0.69
HAFe005.0	4.03	14.58	0.68	0.05	0.12	5.00	0.01	3.83	0.30	3.35	15.76	0.46	0.34	0.21	0.20	50.24	0.14	0.03	0.67
HAFe007.1	3.94	14.26	0.67	0.05	0.12	7.13	0.01	3.74	0.29	3.28	15.96	0.45	0.33	0.20	0.19	49.12	0.14	0.03	0.66
HAFe010.0	3.82	13.82	0.65	0.05	0.11	10.00	0.01	3.62	0.28	3.18	14.93	0.44	0.32	0.20	0.19	47.60	0.13	0.03	0.64

Table 4b
Analysed oxide compositions of the HAFe series samples.

Sample ID	Analysed oxide composition (mol %)[a]																		
	Al_2O_3	B_2O_3	CaO	CeO_2	Cr_2O_3	Fe_2O_3	La_2O_3	Li_2O	MgO	MnO_2	Na_2O	NiO	P_2O_5	PbO	SO_3	SiO_2	SrO	ZnO	ZrO_2
HAFe000.0	3.87 (± 0.08)	16.03 (± 0.44)	0.76 (± 0.02)	0.05 (± <0.01)	0.13 (± <0.01)	0.00 (± 0.00)	0.00 (± 0.00)	3.36 (± 0.13)	0.40 (± 0.01)	3.59 (± 0.07)	16.95 (± 0.35)	0.51 (± 0.01)	0.34 (± 0.01)	0.22 (± <0.01)	0.27[b]	52.56 (± 0.01)	0.13 (± <0.01)	0.00 (± 0.00)	0.82 (± 0.02)
HAFe001.0	4.46 (± 0.09)	12.48 (± 0.36)	0.70 (± 0.01)	0.00 (± 0.00)	0.14 (± <0.01)	1.07 (± 0.02)	0.00 (± 0.00)	3.07 (± 0.12)	0.00 (± 0.00)	4.58 (± 0.10)	17.14 (± 0.37)	0.51 (± 0.01)	0.35 (± 0.01)	0.24 (± 0.01)	0.29[b]	53.86 (± 0.01)	0.14 (± <0.01)	0.16 (± 0.00)	0.81 (± 0.02)
HAFe003.0	4.32 (± 0.09)	12.81 (± 0.37)	0.73 (± 0.02)	0.00 (± 0.00)	0.15 (± <0.01)	3.15 (± 0.07)	0.03 (± <0.01)	3.14 (± 0.13)	0.45 (± 0.01)	3.59 (± 0.08)	16.39 (± 0.35)	0.52 (± 0.01)	0.36 (± 0.01)	0.23 (± <0.01)	0.29[b]	52.76 (± 0.01)	0.13 (± <0.01)	0.13 (± 0.00)	0.78 (± 0.02)
HAFe005.0	3.99 (± 0.08)	15.27 (± 0.42)	0.62 (± 0.01)	0.00 (± 0.00)	0.13 (± <0.01)	4.91 (± 0.10)	0.00 (± 0.00)	3.46 (± 0.13)	0.00 (± 0.00)	4.19 (± 0.09)	15.06 (± 0.31)	0.48 (± 0.01)	0.33 (± 0.01)	0.22 (± <0.01)	0.29[b]	50.13 (± 0.01)	0.20 (± <0.01)	0.00 (± 0.00)	0.71 (± 0.01)
HAFe007.1	4.99 (± 0.10)	11.52 (± 0.31)	0.84 (± 0.02)	0.00 (± 0.00)	0.13 (± <0.01)	8.58 (± 0.17)	0.00 (± 0.00)	2.48 (± 0.09)	0.65 (± 0.01)	3.47 (± 0.07)	12.53 (± 0.25)	0.47 (± 0.01)	0.34 (± 0.01)	0.23 (± <0.01)	0.30[b]	52.78 (± 0.01)	0.12 (± <0.01)	0.00 (± 0.00)	0.58 (± 0.01)
HAFe010.0	3.82 (± 0.08)	14.25 (± 0.40)	0.58 (± 0.01)	0.00 (± 0.00)	0.17 (± <0.01)	10.92 (± 0.23)	0.00 (± 0.00)	3.31 (± 0.13)	0.00 (± 0.00)	4.20 (± 0.09)	13.94 (± 0.29)	0.57 (± 0.01)	0.29 (± 0.01)	0.19 (± <0.01)	0.32[b]	46.63 (± 0.01)	0.12 (± <0.01)	0.00 (± 0.00)	0.68 (± 0.01)

[a] Lithium and Boron were analysed using ICP-MS, the rest were analysed using XRF.
[b] Nominal values used in calculating normalised mol %.

Table 5
XPS target signals and associated energy ranges of the target spectra.

Target signal(s)	Energy range (eV)	Number of sweeps
C 1s	279 - 299	4
B 1s	184 - 210	20
Si 2p	98 - 110	12

Table 6
Measured densities of all samples, standard error given in brackets.

Sample ID	Density (g cm^{-3})	Sample ID	Density (g cm^{-3})
SCFe000.0	2.519 (± 0.008)	CCFe000.0	2.494 (± 0.003)
SCFe000.1	2.520 (± 0.005)	CCFe001.0	2.534 (± 0.003)
SCFe000.2	2.518 (± 0.001)	CCFe003.0	2.554 (± 0.013)
SCFe000.5	2.521 (± 0.001)	CCFe005.0	2.595 (± 0.011)
SCFe001.0	2.534 (± 0.003)	CCFe007.5	2.653 (± 0.011)
SCFe002.0	2.558 (± 0.009)	CCFe010.0	2.699 (± 0.009)
SCFe003.0	2.582 (± 0.005)	HAFe000.0	2.607 (± 0.016)
SCFe004.0	2.584 (± 0.003)	HAFe001.0	2.614 (± 0.014)
SCFe005.0	2.607 (± 0.001)	HAFe003.0	2.646 (± 0.010)
SCFe007.5	2.655 (± 0.003)	HAFe005.0	2.685 (± 0.004)
SCFe010.0	2.688 (± 0.004)	HAFe007.1	2.694 (± 0.002)
SCFe014.0	2.750 (± 0.002)	HAFe010.0	2.731 (± 0.014)

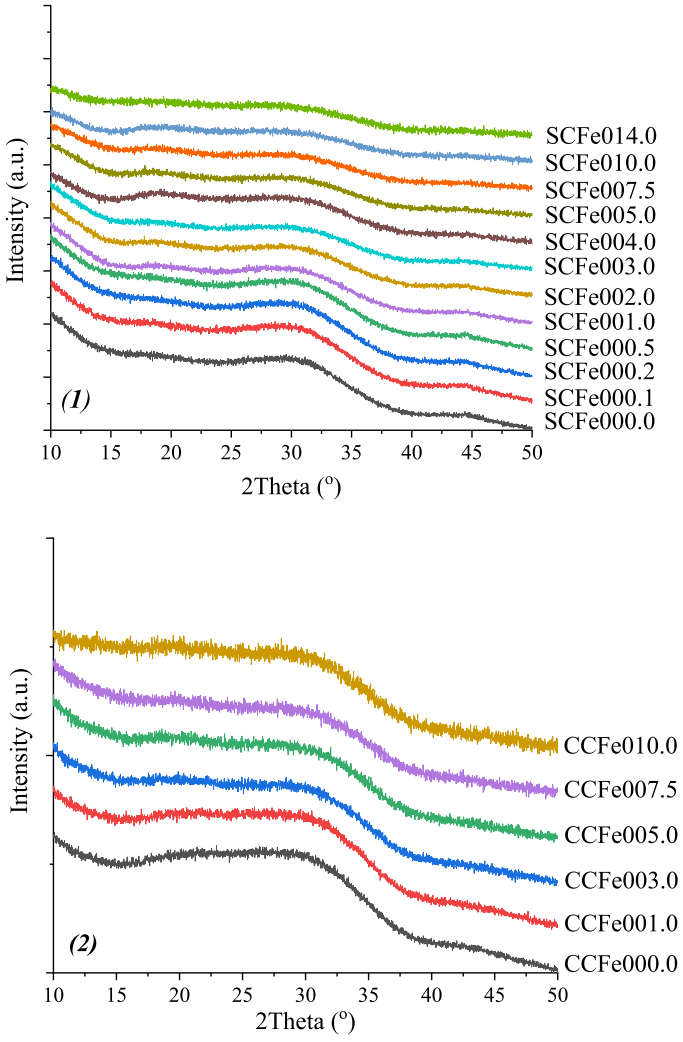

Fig. 1 and 2. XRD patterns for the SCFe and CCFe series.

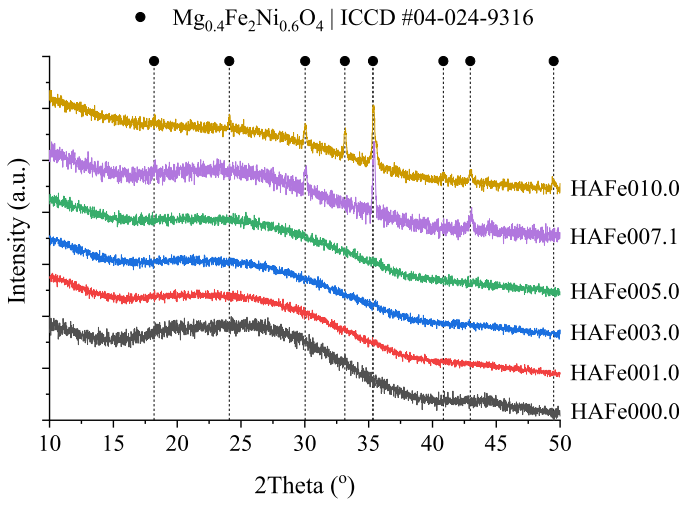

Fig. 3. XRD stack plot for the HAFe series. The spinel phase denoted by the lines is present in the HAFe007.1 and HAFe010.0 samples.

increases, which indicates that between 5 mol % and 7.1 mol % Fe_2O_3 is the solubility limit in the HAFe series glasses, when prepared under the conditions used in this study.

While Highscore Plus software identified a specific spinel phase, due to the presence of a variety of spinel forming components, the exact spinel phase composition provided by the peak fitting software cannot be assumed to be exact. Spinel phases are made up of a formula of $A^{2+}B_2^{3+}O_4$, whereby several components can occupy the A and B sites, as may be the case for the spinel phases observed here. The A-sites can be occupied by Mg, Ni, Fe, Mn, and Zn, while the B-sites can be occupied by Cr, Fe, Mn, and Al. For the HLW-Ng-Fe2 glass from literature [35,36], there are no spinel crystals in the glass as-prepared, but spinel crystals were shown to form during heat treatments at 800, 850, 900, and 950 °C, all of which were only a few percent in abundance as measured by SEM in research by Matlack et al. [39,40]. The low intensity of the spinel diffraction peaks for the HAFe007.1 sample (the closest in composition to HLW-Ng-Fe2), would suggest a low abundance that is consistent with findings in the referenced reports [39,40]. These peaks intensify as the iron content is further increased (sample HAFe010.0), and, as expected, the primary phase is identified is an iron-bearing spinel phase.

3.3. *^{57}Fe Mössbauer spectroscopy*

Figs. 4–7 show the respective series stack plots of the Mössbauer spectra. All Mössbauer spectra were fitted with a minimum of 2 Lorentzian doublets. For the SCFe series and CCFe series, this was sufficient to robustly fit the entire spectral shape (See Figs. 7 and 8). Whereas in the HAFe series, two of the three spectra required an additional Lorentzian sextet fit, which is fully consistent with the presence of magnetic Fe-bearing structures (see Fig. 9).

The parameters for all fits in the measured spectra are given in Table 7.

All of the paramagnetic doublets are consistent with Fe^{3+} sites, with no Fe^{2+} components present, as given by the low centre shift (CS) values [9,11,18,27,33,35,50-61]. The quadrupole splitting (QS) from all fits presents an element of ambiguity. Tomandl [59] states that octahedral Fe units have a greater symmetry and therefore lower quadrupole splitting values than tetrahedral Fe units. This is supported by several published works (see, for example [33,35,50],). However, a review by Dyar shows that for silicate and borate glasses, a lower QS can be assigned to tetrahedral structures [11], which is also supported by several published works (see, for example, [18,20,55,60]). In either case, all measured spectra in this study require two Lorentzian doublets

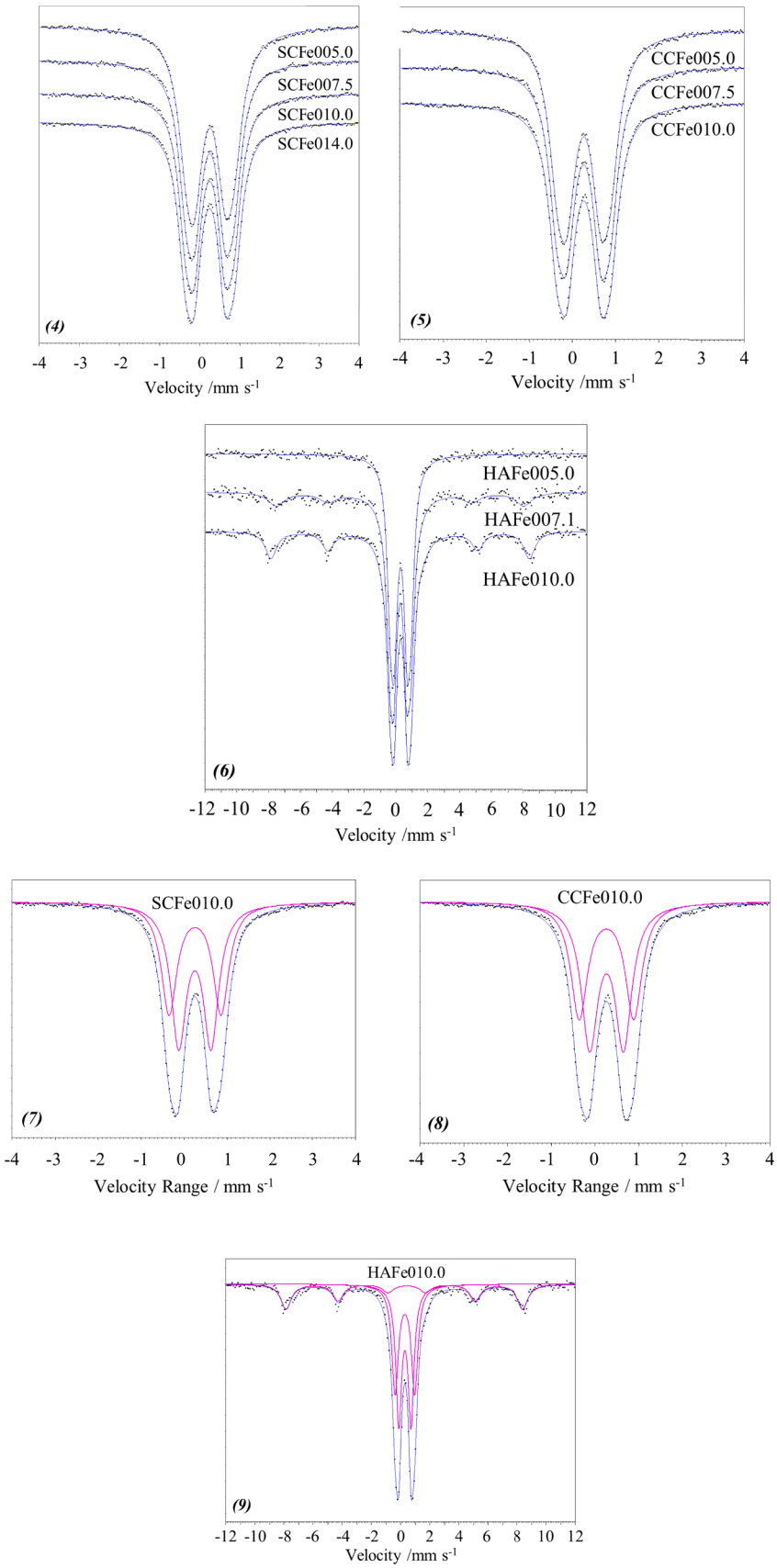

Figs. 4–9. 4) Mössbauer spectra stack plot for the SCFe Series. 5) Mössbauer spectra stack plot for the CCFE Series. 6) Mössbauer spectra stack plot for the HAFe Series. 7) Mössbauer spectrum of the SCFe010.0 sample, showing two Lorentzian doublets. 8) The Mössbauer spectrum of the CCFe010.0 sample, showing two Lorentzian doublets. 9) The Mössbauer spectrum of the HAFe010.0 series showing the additional Lorentzian Sextet as well as the two doublets.

Table 7
Fitted parameters for the Mössbauer spectra of all samples.

Sample ID	Site type	Centre shift (mm s $^{-1}$) (± 0.02)	Quadrupole splitting (mm s $^{-1}$) (±0.02)	Linewidth (mm s $^{-1}$) (±0.02)	Hyperfine field (T) (±0.5)	Site abundance (%) (±2.0)
SCFe005.0	Doublet	0.26	0.75	0.24	–	52.2
	Doublet	0.27	1.17	0.27	–	47.8
SCFe007.5	Doublet	0.26	0.75	0.23	–	56.2
	Doublet	0.26	1.20	0.23	–	43.8
SCFe010.0	Doublet	0.25	0.75	0.22	–	55.2
	Doublet	0.26	1.21	0.22	–	44.8
SCFe014.0	Doublet	0.25	0.77	0.22	–	54.8
	Doublet	0.26	1.23	0.22	–	45.2
CCFe005.0	Doublet	0.26	0.78	0.25	–	57.6
	Doublet	0.27	1.23	0.25	–	42.4
CCFe007.5	Doublet	0.26	0.78	0.23	–	57.8
	Doublet	0.26	1.25	0.23	–	42.2
CCFe010.0	Doublet	0.26	0.78	0.23	–	54.7
	Doublet	0.26	1.25	0.23	–	45.3
HAFe005.0	Doublet	0.26	0.80	0.24	–	49.0
	Doublet	0.27	1.26	0.26	–	51.0
HAFe007.1	Doublet	0.26	0.78	0.23	–	39.0
	Doublet	0.27	1.33	0.26	–	41.0
	Sextet	0.25	0.02	0.62	48.2	20.0
HAFe010.0	Doublet	0.30	0.84	0.24	–	39.0
	Doublet	0.29	1.34	0.27	–	35.2
	Sextet	0.35	−0.08	0.43	50.4	25.8

to obtain robust fits – one doublet with a higher QS value and one with a lower QS value (both with similar CS values). Both doublets have comparable site abundances with a difference of no more than ~10 % on any given sample.

In the context of borosilicate glasses, Cochain et al. [18] reported that Fe^{3+} in the borosilicate glasses studied all occupied tetrahedral sites, with the reported QS values for Fe^{3+} ranging from 0.46 to 0.96 mm s $^{-1}$. However, it is worth noting that the justification for this assignment of coordination was made on the low CS values for all Fe^{3+} doublets (0.25–0.32 mm s $^{-1}$). Nishida et al. [55] reported that lower QS values contributed to tetrahedral structures for Fe^{3+} in iron-bearing potassium borosilicate glasses. The reported QS values had a range of 0.78–1.04 mm s $^{-1}$ and are comparable to the QS doublets obtained here (Table 7). Ciżman et al. [20] report a that a low CS doublet of 0.22–0.28 mm s $^{-1}$ with QS values of 0.74 mm s $^{-1}$ were attributed to tetrahedral Fe^{3+}, though similarly to Cochain et al. [18], this justification was made on the basis of CS values and it was noted that the low QS value could indicate the presence of distorted octahedral Fe^{3+}. In another report, Ciżman et al. [60] reported tetrahedral Fe^{3+} with QS values ranging from 0.91 to 0.94 mm s $^{-1}$. However, Glazkova et al. [35] reported that Fe^{3+} doublets with QS values 0.36–0.92 mm s $^{-1}$ corresponded to octahedral Fe^{3+} in Fe-bearing complex HLW glasses. Forder et al. [61] discussed the hyperfine parameter ambiguity when investigating glasses using Mössbauer and XANES spectroscopy, in that there is more of tendency to observe distorted structures within glass due to a distribution of Fe-O bond lengths and angles. It is reported that distorted 4-, 5- and 6-coordinated iron structures can have overlapping hyperfine parameters within Mössbauer spectra, which is further noted by several authors [18,20,60,61]. When considering the CS of all sites (Table 7), it is concluded that the iron exists in tetrahedral Fe^{3+} sites with varying degrees of distortion brought on by the nature of glass network. While the presence of higher-coordinated ($^{[5\ or\ 6]}Fe^{3+}$) sites is plausible (particularly based on the QS values for some of the doublets), the low CS values suggest that all fitted doublets are consistent with tetrahedral Fe^{3+} sites [9,11,18,27,50-61]. It is therefore suggested that the iron exists predominantly (but not necessarily wholly) as distorted $^{[4]}Fe^{3+}$units within the glass, with no measurable levels of Fe^{2+} within any of the measured samples.

3.4. Fe K-edge XANES

The Fe K-edge XANES spectra for the mineral standards were normalised using the ATHENA software, and then the 1 s – 3 s pre-edge peak at approximate 7111–7114 eV [62,63] (see Figs. 10 and 11) was fitted with a background and several Gaussian peaks (see Fig. 12). For the glass samples, three Gaussian components were used as per the work done on silicate glasses by Farges et al. [62], while the amount of Gaussian peaks fitted to the mineral standard varied depending on the mineral itself. The number of Gaussian components fitted for each mineral was guided by work done on Fe-minerals by Wilke et al. [63], for example, the Fe-berlinite spectrum was fitted with 1 Gaussian peak [63], while the spectrum for magnetite was fitted with 3 Gaussian peaks [63].

The number of Gaussian components fitted were guided by Farges et al. [62] and Wilke et al. [63]. The average centroid positions for the pre-edge peak are calculated using Eq. (6).

$$X_{Average} = \frac{\sum a_i x_i}{\sum a_i} \quad (6)$$

Where a is the area of the Gaussian, i, and x is the position of Gaussian, i. The centroid positions for all measured sample and standard spectra are plotted in Fig. 12. Furthermore, the average centroid positions for more mineral standards were selected from literature to increase the number reference markers available for data processing. The mineral standards selected for Fe^{3+}were Fe-berlinite ($FePO_4$) [63] and ferriorthoclase (Fe: $KAlSi_3O_8$) [63,64] (both 4-coordinated Fe^{3+}), and yoderite ($(Mg,Fe,Al)_8Si_4(O,OH)_{20}$) [63,65] (5-coordinated Fe^{3+}). The mineral standards selected for mixed Fe^{3+} and Fe^{2+} minerals were magnetite (Fe_3O_4) [63] and franklinite ($(Zn,Mn^{2+},Fe^{2+})(Fe^{3+},Mn^{3+})_2O_4$) [63]. The mineral standards selected for Fe^{2+} were wüstite (FeO) [63,66] (6-coordinated Fe^{2+}) and grandidierite ($(Mg,Fe)Al_3(BO_4)(SiO_4)O$) [67] (5-coordinated Fe^{2+}). The mineral references selected from literature combined with the measured mineral standards, ensured that there was at least one mineral for 4-, 5-, and 6-coordinated Fe^{2+} and Fe^{3+}, as well as examples of mixed valence minerals to compare with glass sample spectra. The layout of Fig. 13 was deliberately similar to that of Wilke et al. [63] due to the effectiveness of the layout and to enable comparison. The error bars were derived from similar work done by Feige et al. [68] and Wilke et al. [69] (details in the figure caption of Fig. 13).

Within Fig. 13, the average centroid energy is the predominant determining factor for oxidation state of the iron, whereas the integrated intensity is indicative of the coordination number for the iron (both trends are broadly followed by the mineral standards) [70–72]. For each

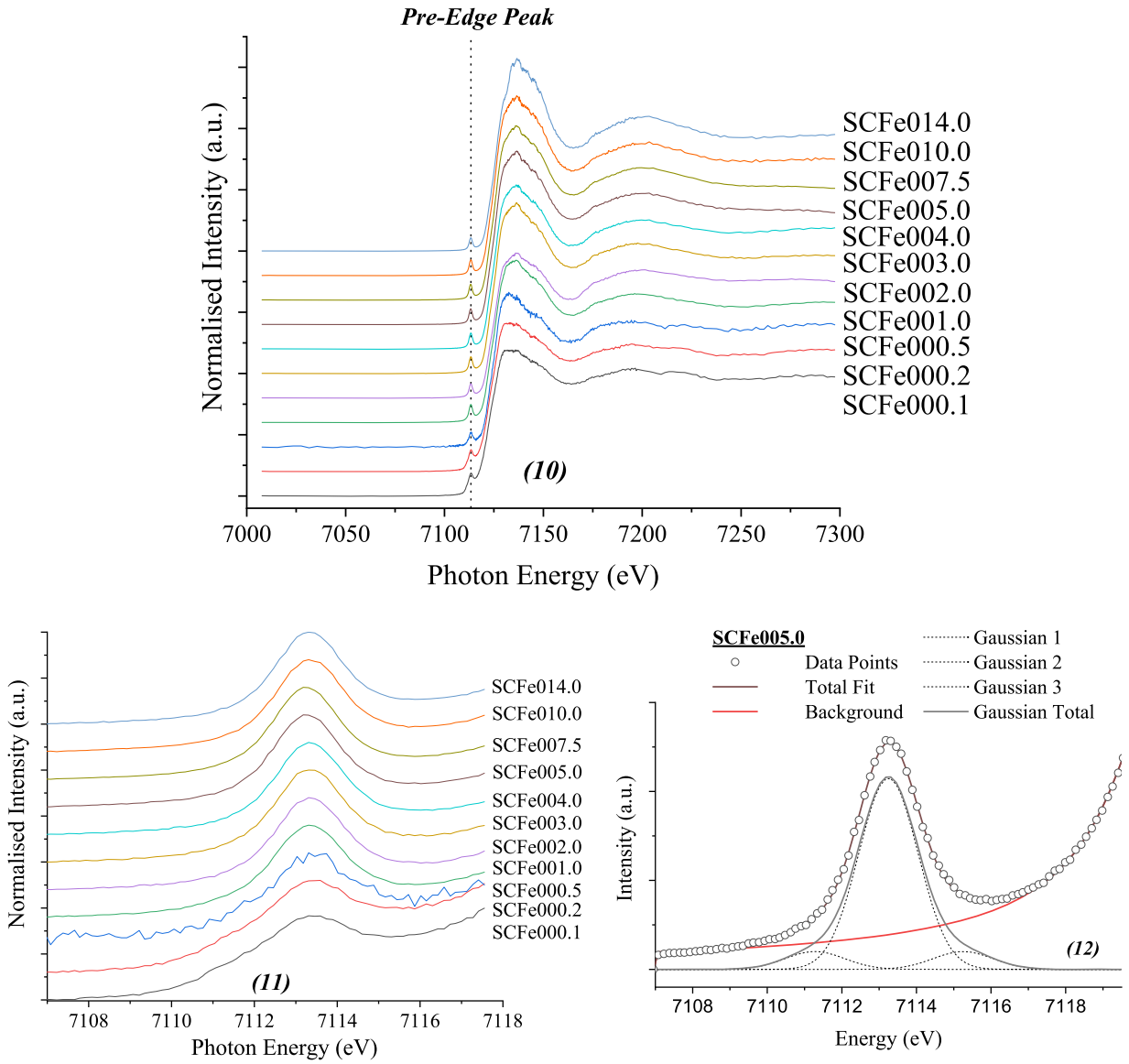

Figs. 10–12. Fig. 10 shows the stack plot of the SCFe series, with the pre-edge peak marked on all spectra. Fig. 11 shows the SCFe series as an example stack plot of the pre-edge 1 s–3 s peak. Figure 12 shows the SCFe005.0 sample pre-edge peak with 3 fitted Gaussian peaks – similar fits were used for all samples.

series, these trends can be seen more closely in Figs. 14–16.

For most glass samples the valence of the iron obtained from the XANES pre-edge peak data is consistent with all iron being present as Fe^{3+}, with the exception being three HAFe samples with peaks centred at approximately 7112.9 eV. This might suggest the presence of some level of Fe^{2+} within these three samples when compared to the centroid energy of magnetite (Fe_3O_4)… This result is consistent with similarly reported XANES data for Fe-bearing silicate and phosphate glasses [17, 59,73–78]. For example, Berry et al. [78] studied the REDOX of iron in silicate glasses using Fe K-edge XANES and ^{57}Fe Mössbauer spectroscopies. Their glass sample in which the iron corresponded to theoretically 100 % Fe^{3+} had a XANES pre-edge peak centroid energy 0.9 eV lower than the centroid energy for their haematite (Fe_2O_3) sample [78]. Considering this difference of 0.9 eV between the centroid energies for the haematite and 100 % Fe^{3+} glass samples in Berry et al. [78], this is directly equivalent to the centroid energy difference between the haematite sample and the three HAFe glasses shown in Fig. 13. It is also notable that the difference in centroid energies found by Berry et al. [78] for magnetite (Fe_3O_4) and their 100 % Fe^{3+} glass sample, was only 0.15 eV, i.e. their centroid energies were almost identical, which is also found here for the HAFe001.0, 003.0 and 005.0 samples. Furthermore, the Mössbauer spectral parameters found in this study for these three HAFe samples (see Figs. 4–9and Table 7) all indicated that there is no detectable Fe^{2+} and that, within uncertainties, all iron exists as Fe^{3+}. Given the distinct lack of an Fe^{2+} doublet in the Mössbauer spectrum for the HAFe005.0 sample (Fig. 6), it is highly unlikely that the HAFe samples contain measurable levels of Fe^{2+}. In light of this, and the known accuracy of determining iron redox using Mossbauer spectroscopy compared with XANES [79], our Mössbauer data will be given greater weight when discussing the iron chemistry of the HAFe glass series.

The integrated XANES pre-edge peak intensities for all glass samples suggests that the Fe-O coordination number ranges from 4 to 5, and that no samples have an integrated intensity low enough to suggest significant quantities of 6-coordinated Fe. However, this does not rule out the possibility of some mixture of 4-, 5- and 6-coordinated Fe. Magnetite (Fe_3O_4) consists of 4-coordinated Fe^{2+} and 6-coordinated Fe^{3+} [80] and the plotted integrated intensity for magnetite is comparable to many of the sample data points, again suggesting a mixture of 4- to 6- coordinated Fe sites in the glasses. Consequently, for these samples, the Fe

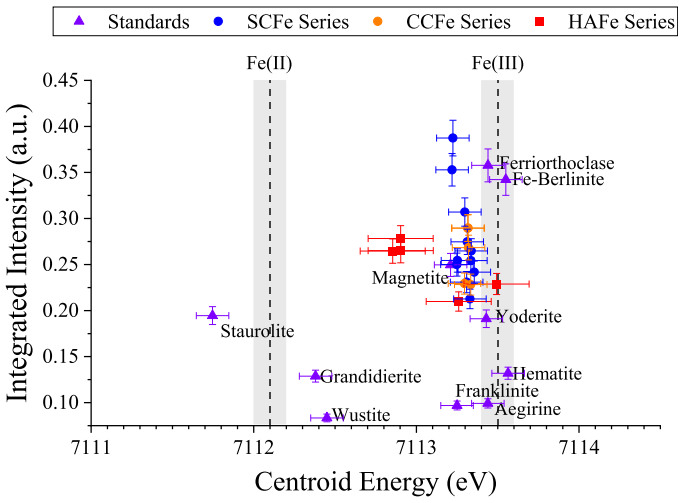

Fig. 13. Average Fe K-edge XANES pre-edge centroid energy positions for all samples and standards. The x-axis error bars are +/- 0.1 eV on the centroid energy (per Feige et al. [68]) for the SCFe and CCFe sample series, and +/- 0.2 eV for the HAFe series due to the larger step size used in acquiring the spectra. The y-axis error bars are +/- 5 % of the value on the integrated intensity (per Wilke et al. [69]). Grey regions around the Fe(II) and Fe(III) lines indicate the +/- 0.1 eV uncertainty on these positions.

K-edge XANES data is only qualitative in providing average Fe-O coordination numbers for the glasses [61,79]. This is comparable to what can be concluded regarding Fe-O coordination from the Mössbauer data, with both techniques consistent with iron being present in all glasses as only Fe^{3+}, and with an average Fe^{3+}-O coordination number between 4 and 5.

3.5. Raman spectroscopy

The normalised Raman spectra for all three sample series are shown in the stack plots in Figs. 17–19. The stack plots show significant structural changes arising within each series, across the spectral region of interest (200–1600 cm^{-1}).

The Raman spectra for all three sample series can be split into in the 3 regions – the low-frequency region (200–800 cm^{-1}), the mid-frequency region (800–1200 cm^{-1}), and the high-frequency region (1200–1600 cm^{-1}). The low frequency region is predominantly dominated by various stretching modes of the silicate network [81–83], with some mixed borosilicate bands [84,85], and borate bands [84,86-90] towards the upper limits of this region. The mid-frequency region is dominated by symmetrical stretching of the various tetrahedral units within the respective series (e.g. SiO_4, AlO_4, FeO_4) [90–93]. The higher frequency region shows predominantly metaborate bands [84,88,90,94–98]. Across all three sample series, the stack plots show large changes in the mid-frequency region, and also changes in the high- and low-frequency regions. To illustrate these changes, Raman Difference Spectra (RDS) were generated for each series, by subtracting the normalised spectrum for the iron-free glass from each series from the normalised spectrum for each subsequent sample. This provides the RDS, which shows the change in spectral features due to increasing levels of Fe_2O_3 incorporation in the samples. The RDS are shown in Figs. 20–22.

The RDS confirm the changes observed in the stack plots, and show that the changes occur stepwise as the Fe content of the glass increases. For the SCFe and CCFe series, there appears to be a reduction in a specific band at approximately 630 cm^{-1} and the same band decreases in intensity in the HAFe series, but the change is less consistent, and in the case of sample HAFe007.1, there is a sharp increase in the intensity of a band at approximately 600 cm^{-1}. A band at this Raman shift has been previously attributed to borosilicate ring structures with compositions

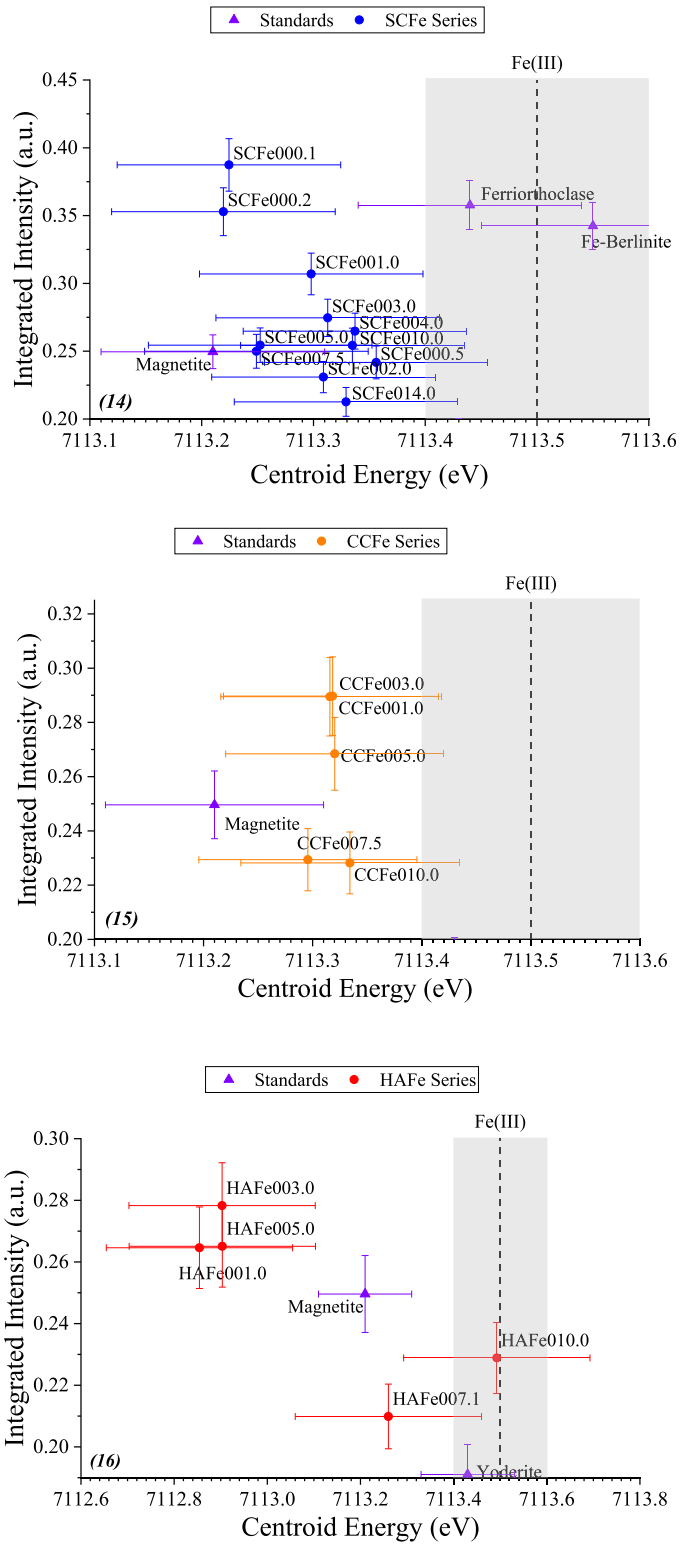

Figs. 14–16. Integrated Fe K-edge XANES pre-edge peak intensities as functions of centroid energies for individual sample series. Error bars are the same as the ones used in Fig. 13.

analogous to danburite and reedmergenerite [82].

In the mid-frequency region, with increasing Fe content there is a decrease in the higher frequency bands with a simultaneous increase in lower frequency bands in all three series. This suggests a progressive shift in configuration of the contributing bands in this region. In simpler glass matrices, this would be attributed to a combination of shifting to

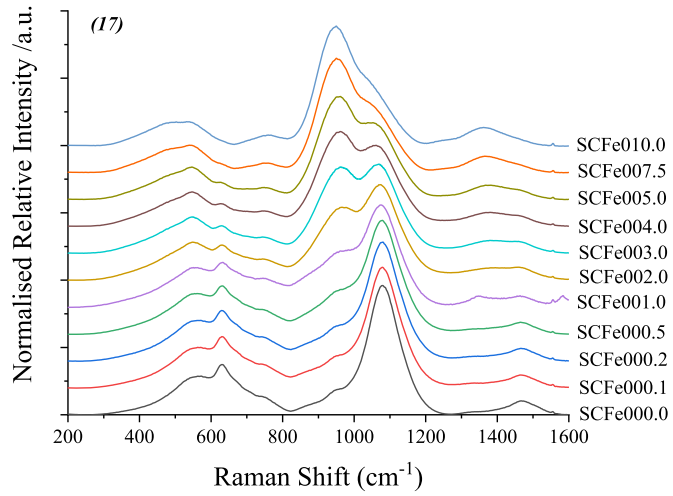

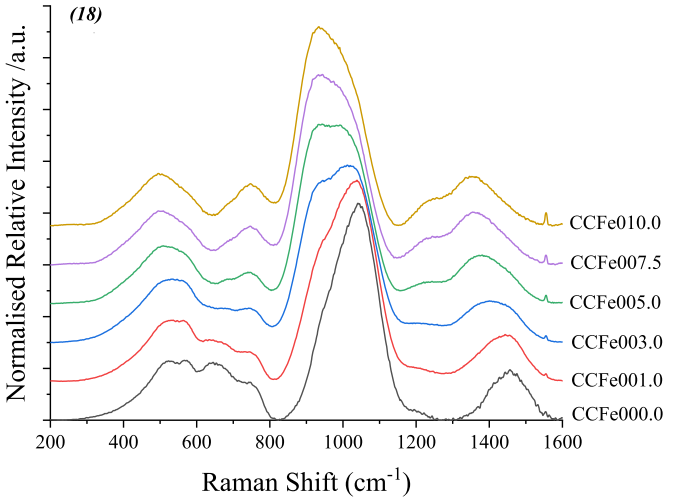

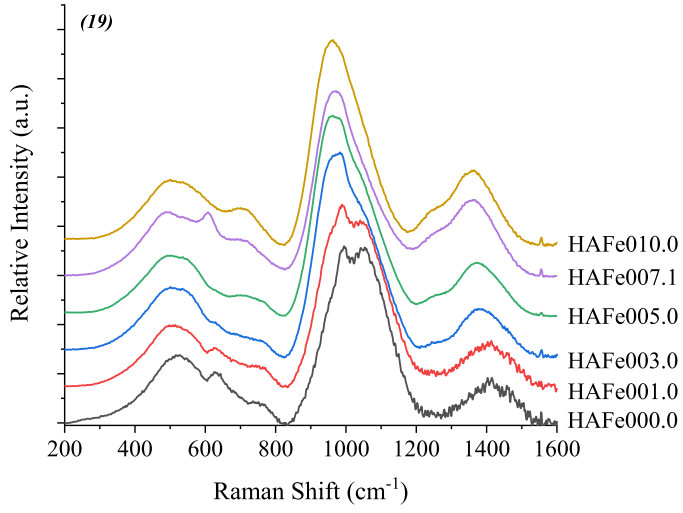

Fig. 17–19. Raman stack plots for all three glass series: 17) SCFe Series, 18) CCFe Series, and 19) HAFe Series.

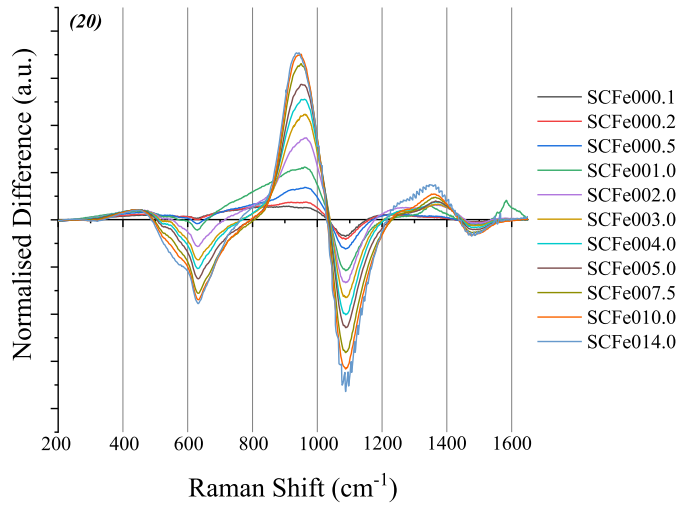

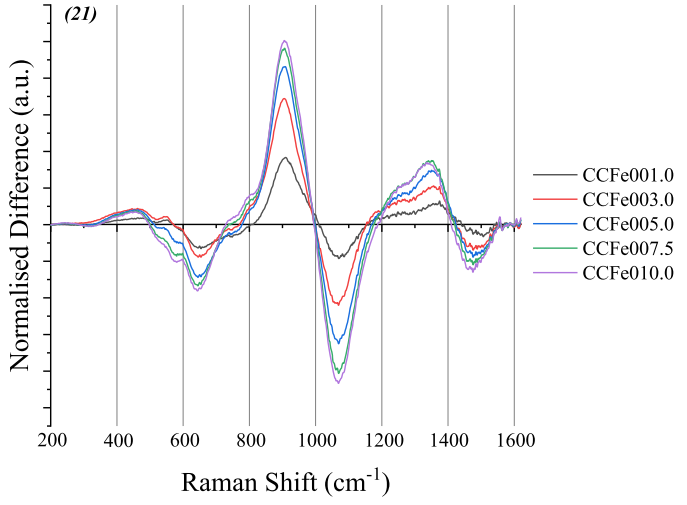

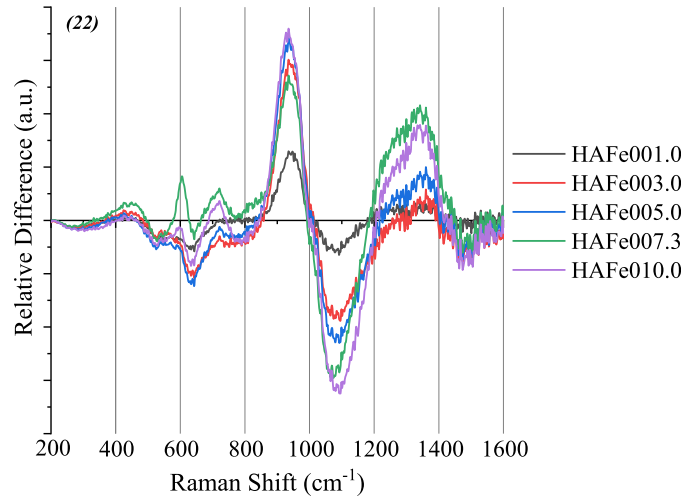

Fig. 20–22. Raman Difference Spectra (RDS) plots for each sample series.

lower Q-species (fewer bridging oxygens per network tetrahedron) [91], as well a potential change in modifier configuration [99]. However, due to the complex nature of the glass series' investigated in this study, deconvoluting exactly what is having the most impact in this region is incredibly difficult owing to overlapping contributions from many different species.

In the higher frequency region, with increasing Fe content there is a similar effect to that of the mid-frequency region, with the increase in lower frequency bands being more prevalent in the HAFe series. The lower frequency bands have been attributed to "loose" BO_3 groups [96,

98] (defined as "loose" due to not being bound in metaborate structures), while the higher frequency bands have been previously attributed to mixed metaborate groups, such BO_3 bonded to BO_4 groups, and BO_3 bonded to other BO_3 groups [94].

In the context of iron additions to glasses, Cochain et al. [18] observed a similar shift in the mid-frequency region towards lower frequency bands with increasing Fe content. This was attributed to a band emerging at around 980 cm^{-1} as the iron contents increased, with the band being attributed to 4-coordinated Fe^{3+} (Fe-O bonds) based on work by Magnien et al. [100]. This effect can be seen within the stack plots and RDS for all three series (Figs. 17–22), where there is a band emerging around 980 cm^{-1} as the Fe_2O_3 contents increase in the series. Welsch et al. [101] also reported this same band in a study of trisilicate glasses with varying modifier cations. They noted that it varied in position with changing modifier cation (Li, Na, and K were studied), from 980 cm^{-1} for Li-bearing glass to 1000 cm^{-1} for K-bearing glass. Furthermore, Welsch et al. [101] suggests that the band at around 980 cm^{-1} can be attributed to all Fe^{3+} units and not only tetrahedral Fe^{3+}, which is a development on the original assignment described in Cochain et al. [18] and Magnien et al. [100]. Le Losq et al. [102] studied aluminosilicate basalt glasses and used Raman spectroscopy to determine the iron redox ratio with in the glasses and compared the results to Mössbauer spectroscopy results for the same glass from a previous study [103]. It was found that the intensity of this peak correlated linearly with the redox ratio calculated using Mössbauer spectroscopy. Balasubramanya et al. [104] reported a similar Raman peak in a complex, transition metal-rich borosilicate glass system and found that while sodium preferentially charged compensated Fe^{3+} tetrahedral groups, lithium and calcium preferred to form ionic bonds through the silicate and borate networks, and as such, the iron was more likely to reduce in high-Li and high-Ca glasses, if there was not enough Na to sufficiently charge compensate the tetrahedral Fe^{3+} and saw a corresponding reduction in intensity for this particularly Fe^{3+} band. Rigby et al. [105] reported on the changes in Raman band intensity for the peak at approximately 630 cm^{-1} when looking at the effect of different reductants on the melting behaviour of high-Fe Hanford wastes. It was reported that as the abundance of Fe^{3+} increases within the samples (as measured with Mössbauer spectroscopy), there is a noticeable decrease in the intensity of this band, a trend that is also seen in this study for all three glass series.

3.6. B K-edge xanes

The normalised spectra are plotted as stack plots for the two series in Figs. 23 and 24.

Boron K-edge XANES spectra can be described by three peaks. Peak A at approximately 194.5 eV depicts the electron transition to an unoccupied 2p orbital that is typical only permissible to $^{[3]}B$ structures [106]. Peak B at approximately 198 eV is attributed to a transition to unoccupied σ states that are forbidden in $^{[3]}B$ structures but permissible in $^{[4]}B$ structures [105]. Peak C at approximately 202 eV describes diffuse contributions from both $^{[3]}B$ and $^{[4]}B$ *s* electrons transitioning to σ bands [106]. These peaks were fitted with a linear background and 3 Gaussian peaks (a similar method to one employed by Fleet & Muthupari [107], Sauer et al. [108], and Garvie et al. [109]). The peaks for each sample were processed using Eq. (7), similar to the one used by Fleet & Muthupari [107], to produce semi-quantitative values for the fraction of $^{[4]}B$ in each of the measured samples.

$$^{[4]}B = \frac{Area_B}{Area_A + Area_B} \tag{7}$$

The $^{[4]}B$ abundance is plotted in Fig. 25 for the two measured series.

Fig. 25 shows that in both series, increasing Fe_2O_3 content has little impact on the boron coordination, which is somewhat more strongly affected by base glass composition. There is a trend that suggests the $^{[4]}B$ abundance slightly decreases as Fe_2O_3 content increases but these changes are modest. It also shows that, predictably, the CCFe series starts with less $^{[4]}B$ than the SCFe series, likely due to the presence of AlO_4^- tetrahedra that will be preferentially charge compensated by

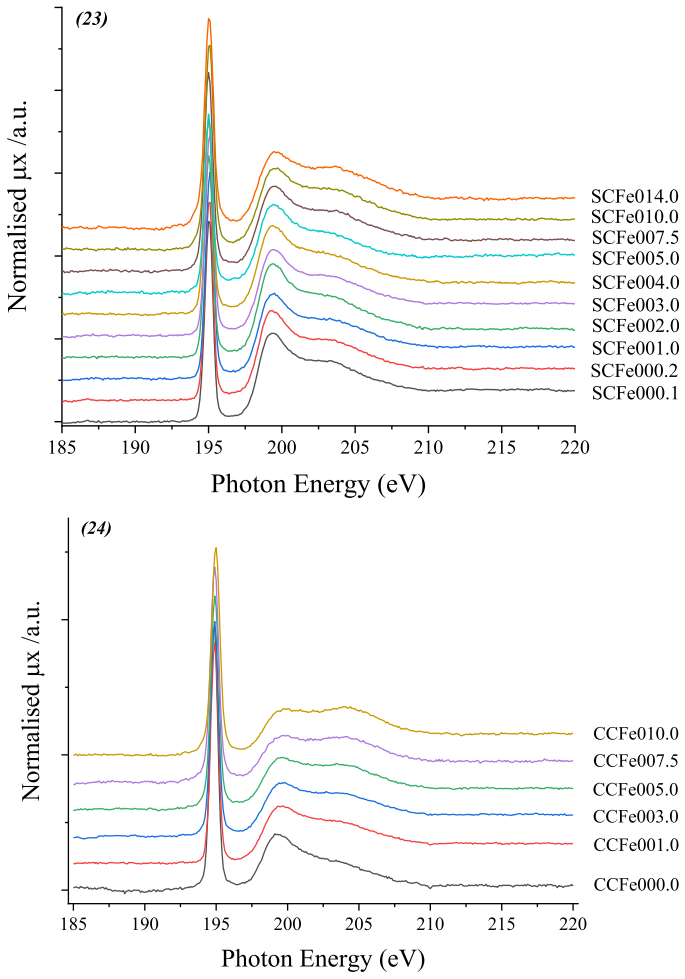

Fig. 23 and 24. Boron K-edge XANES stack plots for SCFe and CCFe sample series.

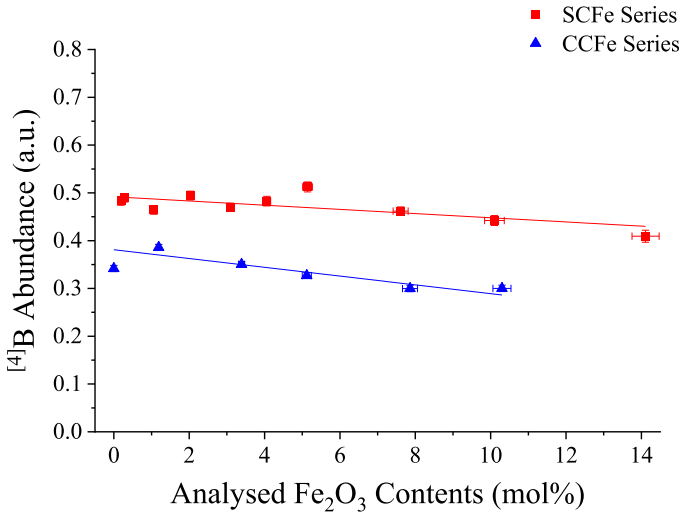

Fig. 25. $^{[4]}B$ abundance from B K-edge XANES fitting for both sample series. Linear fits added as a guide only.

modifier cations before both the $^{[4]}B$ and Fe^{3+} tetrahedra [18,26,110]. A similar lack of effect on the $^{[4]}B$ abundance as a function of increasing Fe contents within the glass was also reported by Cochain et al. [18].

The abundance of $^{[4]}B$ in the glass for the SCFe series between 50–60 % of the total boron content is consistent with estimates from published research such as the Yun, Bray, and Dell model [111–113] for a borosilcate glass with an R value range (Na_2O / B_2O_3) of 1.58–1.70 and K value range (SiO_2 / B_2O_3) of 3.23–3.50, as is the case for the SCFe series. Further coroboration can be found in B XANES results published by Li et al. [114] who studied K_2O-SiO_2-B_2O_3-P_2O_5 glasses, in which comparable compositions were found to contain approximately 50–55 % of the total boron as $^{[4]}B$, which compared the values against NMR data in good agreement [115].

3.7. X-ray photoelectron spectroscopy (XPS)

The centre position for the B 1 s spectra for both series was plotted as a function of changing Fe_2O_3 contents within the glass (the B 1 s stack plot can be seen in Figs. S11 and S12 of the supplementary material). This was determined by fitting a single Gaussian peak for each spectrum and plotting the centre values for each peak against the iron oxide content within the sample. This data is presented in Fig. 26.

The data shows a gradual decrease in binding energy for the 1 s electron as the concentration of Fe_2O_3 increases within the sample. For both series, there is an approximate 0.6 eV change in binding energy between the start and end members of both series. The nature of this change is change is discussed later in this section.

Similar to the B 1 s, the centroid binding energy for the Si 2p was plotted as a function of changing Fe_2O_3 content (the Si 2p stack plots can be seen in Figs. S13 and S14 in the supplementary material). This was carried out by fitting a single Gaussian peak to the signal and plotting the centre position. It is acknowledged that any 2p signal typically needs to be fitted with two peaks, to represent the 1/2 spin and 3/2 spin with a fixed distance (0.6 eV for Si 2p [116]) and an area ratio of 0.5 with the higher energy 3/2 with the lower area [117]. However, when dealing with small energy split values for 2p doublets, it can fit with a single component. An example of this, can be seen in a book by Watts & Wolstenholme [117] on the Al 2p spectrum (specifically Fig. 3.5 in the reference [117]). The peak binding energies for the Si 2p signals are given in Fig. 27.

Miura et al. [118] used XPS to investigate the O 1 s, Si 2p, B 1 s, and Na 1 s signals to characterise the bridging oxygens and non-bridging oxygens within simple sodium borosilicate glasses, comparable to the SCFe series in this study. They reported that there is a shift to a lower

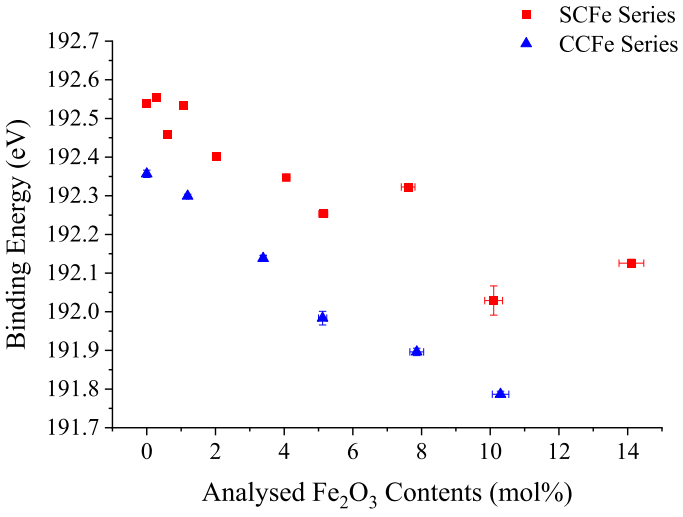

Figs. 26. XPS B 1 s binding energy as a function of Fe_2O_3 content for CCFe and SCFe sample series.

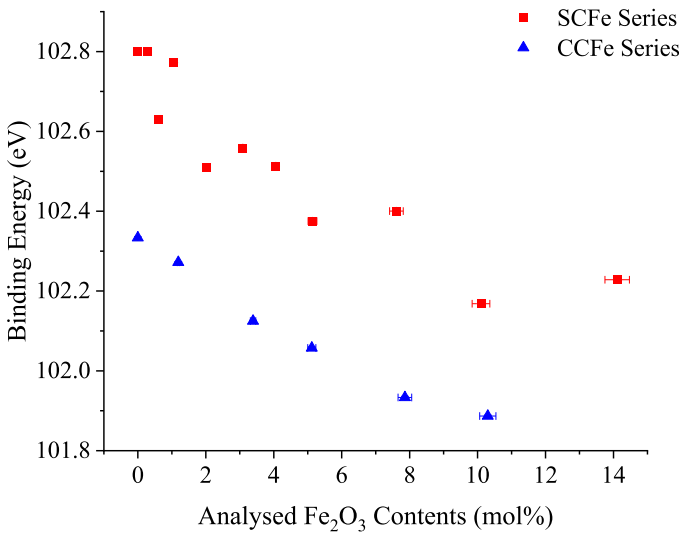

Figs. 27. XPS binding energies of Si 2p signals for both series.

binding energy in the B 1 s, Si 2p, and Na 1 s as the amount of sodium increased in the studied series. This was linked to the optical basicity of the glass and the authors discussed how this could be used to predict the likelihood of a BO_3 or BO_4 group forming through interactions with the silicate network, improving understanding of how a borosilicate glass network forms beyond the Yun, Bray, Dell, Xiao model [111–113]. Mekki et al. [119] studied Fe_2O_3 substitutions into sodium silicate glasses. It was found that the Fe 3p signal could be used to assess the iron redox ratio and the Si 2p had a corresponding reduction in binding energy. This reduction in binding energy was attributed to more non-bridging oxygens on the Si tetrahedra within the glass. As the oxygen forms bonds with a greater ionic character, it relaxes the attraction to the Si electrons in the covalent bonds in forms with the Si cation [120]. Holland et al. [121] built on the XPS work by Mekki et al. [119] to show that the Si-O-Fe bond has its own unique signal in O 1 s due to the difference in bond length and, by association, difference in covalent character of the bond. It was shown to have a higher binding energy than the Si-O-Na bond, but lower than that of the Si-O-Si bond. This suggests a greater ionic character to the Fe-O bond than to Si-O, which is consistent with understanding of glass network intermediates as described by Stanworth [122]. While Si and Fe^{3+} have similar electronegativities, 1.8 as given by Gordy and Thomas [123], the ionic radius of Si (1.10 Å [124]) is smaller than Fe^{3+} (1.40 Å [125]) and therefore the Si will form bonds with a greater covalent character [125] and should be reflected in the electron binding energy data in the XPS.

Hsieh *at al.* [126] used changes in the Pauling charge [127] of glass forming constituents in alumino- and boro-trisilicate glasses, with links to binding energy to describe the structural changes within the silicate network. A similar study by Clarke & Rizkalla [128] considered different silicate glasses and materials. Both studies found a linear relationship between binding energy in the O 1 s and Si 2p spectra. Brow & Pantano [129] (also used in further work by Brow & Pantano [130]) found a similar relationship between the Si 2p and O1s in silicon oxynitride thin films and described it using Eq. (8).

$$\Delta(BE_i) = k\Delta q_i \tag{8}$$

Where $\Delta(BE_i)$ is this change in binding energy of the measured cation, i, k is a proportionality constant, and Δq_i is the change in net charge of the cation, i. Hsieh et al. [126] noted that while Brow & Pantano's [129, 130] approach did utilise a coordination factor, Clarke & Rizkalla's [128] does not, but the latter's approach considers the environment of the next nearest neighbour of the target atom where the former does not. For this study, however, Brow & Pantano's linear equation has been

used due to the complexity of the studied glasses. The changes in binding energies for the Na 1 s, Si 2p, and B 1 s signals for both series are shown in Table 8.

Decreases in binding energy in both series across all three signals are thus observed (Table 8). From literature it can be determined that for the glass forming constituents (Si, and B) the bonds forming with these cations have less covalent character as a result of increasing Fe contents. Mekki et al. [119] and Holland et al. [121] indicated that the Fe-O bonds have less covalent character than Si-O bonds. Veal et al. [120], Hsieh et al. [126], Clarke & Rizkalla [128], and Brow & Pantano [129,130] all show that binding energy is proportional to the net charge on a cation and that this net charge is sensitive to change in electronegativity on the neighbouring atoms.

4. Discussion

4.1. Iron chemistry

^{57}Fe Mössbauer and Fe K-edge XANES spectroscopies both show that the iron within all three glass series exists predominantly as distorted $^{[4]}Fe^{3+}$, however, there is a degree of conjecture regarding the precise coordination, or range of site distortions / coordinations, of the Fe^{3+}. This conjecture is also found in a wide body of historical literature, for example in terms of the quadrupole splitting (QS) values from fitting of Mössbauer spectra. In some such studies, the authors have defaulted to using the centre shift (CS) of the fitted parameters to determine coordination [11,18,20]. When considering the XANES data for the three studied glass series (Figs. 13–16), it can be seen that the integrated pre-edge peak intensities for the lower iron samples have values that are clearly consistent with 4-coordinated Fe [62,63] and then gradually decrease towards values more consistent with 5-coordinated Fe as the iron content increases. It is known that in glass, M-O bond angles and bond rotations are not fixed and this distribution of angles and bond rotations lead to distorted structures that manifest as broadening of spectral features across multiple spectroscopies. The XANES data for the low-Fe samples in the SCFe series demonstrate integrated pre-edge peak intensity values consistent with $^{[4]}Fe^{3+}$ (see Figs. 13and 14). These intensities gradually decrease with increasing Fe content towards values more indicative of an average $^{[5]}Fe^{3+}$, which could suggest that the iron is forming tetrahedral groups that are increasingly distorted as iron content increases, as indicated by Forder et al. [61]. The CCFe series and HAFe series glass XANES pre-edge peak data (Figs. 13,15 and 16) show that the low-Fe glass samples produce intermediate integrated pre-edge peak intensities which change little with increasing Fe contents within the glass. These differences in behaviour between the three glass series are also reflected in the Mössbauer QS values for each series relative to one another (see Table 7), where QS values increase with increasing complexity of the glass system (number of different elemental components). However, these QS values are all within a similar range of one another, i.e. any differences are small but non-zero. It is thus suggested that the Fe in each glass series is likely to occur as predominantly distorted $^{[4]}Fe^{3+}$, with the tetrahedral units displaying increasing average distortion with increasing Fe content and system complexity. While the presence of some $^{[5\text{ or }6]}Fe^{3+}$ cannot be ruled out in the any of the three glass series, there is more evidence to suggest that the parameters reflect predominantly distorted $^{[4]}Fe^{3+}$.

Table 8
Binding energy changes in XPS B 1 s and Si 2p for the two measured series.

XPS signal	Binding energy changes, SCFe Series (eV)	Binding energy changes, CCFe Series (eV)
B 1s	−0.414 (± 0.014)	−0.570 (± 0.018)
Si 2p	−0.571 (± 0.003)	−0.447 (± 0.005)

4.2. Glass chemistry

The impacts of increasing the Fe_2O_3 contents on the wider glass chemistry are varied. The boron K-edge XANES data showed that the increasing Fe contents within the glass has only modest impact on the boron coordination, similar to a trend reported by Cochain et al. [18]. However, the Raman data for all three glass series (Figs. 17–22) showed that there are impacts the borate and silicate bands, specifically a decrease in intensity in borosilicate (600 - 800 cm^{-1}) and metaborate bands (1200–1600 cm^{-1}). With the decrease in intensity of the band at approximately 630 cm^{-1} commonly attributed to reedmergenerite- and danburite-like borosilicate ring structures [81,82], the initial theory was that the Fe^{3+} tetrahedral units were potentially being preferentially charge compensated by the modifier cations such as sodium. This caused a conversion from $^{[4]}B$ units to the charge neutral $^{[3]}B$ units, which break up the danburite- and reedmergenerite-like groups [81,82]. This would account for the decrease in intensity for borosilicate Raman bands (600–800 cm^{-1}) as the Fe^{3+} concentration increases, a theory also suggested by Rigby et al. [105]. The boron K-edge XANES data, however, does not support this hypothesis here. Fig. 24 clearly shows that the $^{[4]}B$ abundance is little affected by the increase in Fe contents, and the Mössbauer spectra in Figs. 4–9 show all Fe existing as Fe^{3+}, though a slight decrease in $^{[4]}B^{3+}$ is observed. This would suggest that the boron coordination remains largely unchanged as a function of Fe content, with no clear link between the concentration of Fe^{3+} and the slight change in boron coordination. Therefor an alternative explanation for this trend is required.

To coincide with the changes observed in the Raman spectra, there was a slight decrease in the binding energy of the B 1 s and Si 2p electrons with increasing Fe content, as measured by XPS for the SCFe and CCFe series (Figs. 26 and 27). For the SCFe series, the Si 2p showed a greater decrease in binding energy (Table 8) than the B 1 s binding energy. The CCFe series showed the opposite trend. This would suggest that as Fe content increases, the net charge on the measured cations decreases in accordance with the proportional equation (Eq. (8)) given by Brow and Pantano [129,130]. Clarke and Rizkalla [128] demonstrated that changes in the net charge are sensitive to the bonds formed by the next nearest neighbours in even the simplest systems. Given that the glasses in this study are so much more complex than in the systems studied by Clarke and Rizkalla [128], it would be impossible to determine exactly which changes in bond configurations are those most responsible for the decrease in binding energy. The effects on the Raman spectra show a decrease in the metaborate bands at approximately 1380 - 1490 cm^{-1} [94] while a simultaneous increase in bands at about 1325 cm^{-1} attributed to “loose” BO_3 units, is observed [96,98] (see RDS in Figs. 20–22 for a clearer illustration of this). While in the simpler glass series, it could be suggested that the silicate groups are affected as much, if not more, with the increase in Fe contents, which is consistent with conclusions published by Wright et al. [19] who used EXAFS data and neutron diffraction to quantitatively determine that $^{[4]}Fe^{3+}$ preferentially integrates through the silicate sub-network in a simple sodium borosilicate glass which is comparable to the SCFe series studied here. As the glass becomes more complex, with the addition of CaO, Li_2O, and Al_2O_3, the impact of the increasing Fe content shifts towards the borate sub-network, in accordance with the Raman and XPS data. This data is suggesting that as the Fe^{3+} integrates within the glass matrix it is having a significant effect on the borate groups within the complex borosilicate network. While the glasses are broadly too complex to quantitatively analyse exactly how the Fe^{3+} integrates within the network, qualitatively, it is bonding into the borate sub-network more so than it is bonding into the silicate sub-network as the composition increases in complexity, as evidenced by the changes in the Raman and XPS spectra as a function of increasing iron oxide within the glass. Wright et al. [19] noted that Fe^{3+} can integrate into the borate sub-network in borosilicate glasses, but is more likely to do so as $^{[6]}Fe^{3+}$. Applied to the glasses studied here, this would suggest that there could be an increase in levels

of $^{[6]}Fe^{3+}$ from the SCFe series glasses to the CCFe series glasses. However, the Mössbauer fitting parameters (see Table 7), do not show any significant changes in relative abundances of one doublet type between the two series. Furthermore, the Fe K-edge XANES data in Fig. 13 show that the integrated intensity of the pre-edge peak between the SCFe, CCFe, HAFe sample series are not sufficiently different enough to suggest a measurable change in average Fe coordination between the series. Nevertheless a small and subtle yet non-zero effect must be considered on the basis of these results.

One theory that could also help to explain this effect is the avoidance between tetrahedral species. Du and Stebbins [131] observed tetrahedral avoidance between AlO_4^- tetrahedra and BO_4^- tetrahedra in alkali aluminoborosilicate glasses. Zhang et al. [132] also observed tetrahedral avoidance between AlO_4^- and FeO_4^- tetrahedra in phosphate-free and phosphate-doped alkali aluminoborosilicate glasses. It can thus be hypothesised that if the AlO_4^- tetrahedra avoid BO_4^- tetrahedra and FeO_4^- tetrahedra avoid AlO_4^- tetrahedra, the evidence from this study suggests that FeO_4^- tetrahedra preferentially bond with the borate subnetwork in the complex glasses studied here containing Al_2O_3. Hence this may be a consequence of competition between the relative tetrahedral avoidances suggesting FeO_4^- / AlO_4^- being less likely than FeO_4^- / BO_4^-. Furthermore, Bingham et al. [17] studied the selective behaviour of dilute Fe^{3+} cations in silicate glasses, and found that depending on the alkali or alkaline earth cation type providing charge compensation or bonding with the Fe^{3+} cation, the Fe-O coordination and bond length would change. Qualitatively, it was shown that the lower the ionic radii ratios of the modifier parings modifier (examples given in ref [17]: Li-Ba & Na-Ba), the higher the coordination of the Fe, while the higher the ionic radii ratios (examples given in ref [17]: K-Ca, K-Mg, Na-Mg) the coordination of the Fe was lower [17]. This qualitatively supported findings by Farges et al. [62], which used Fe K-edge XANES and molecular dynamic simulations to study the changes in Fe-coordination and valency as a function of changing modifier cations, which included Ca, Na, Mg, K. Balasubramanya et al. [104] studied the effects of Na, Li, and Ca network modifiers on the spinel crystallisation within complex borosilicate glasses. It was shown that the higher the cation field strength, the greater the depolymerisation, greater the increase in Fe^{2+}, and more likely to promote secondary crystallisation through clustering of Fe, or even LiAl (which forms spodumene). Furthermore, Wiegel et al. [133] used neutron diffraction and Empirical Potential Structure Refinement (EPSR) simulations to show that within $NaFeSi_2O_6$ (NFS) glasses, that while the iron exists predominantly as $^{[4]}Fe^{3+}$, there is also $^{[5]}Fe^{3+}$ and $^{[5]}Fe^{2+}$ species that can form edge-sharing clusters in higher concentrations of Fe within the glass.

When considering the glasses studied in this research, it is likely that the findings by Wright et al. [19] explain why, in the SCFe series glasses, the iron impacts more on the silicate sub-network than the borate sub-network, as the iron exists predominantly as Fe^{3+}. However, within the CCFe and HAFe glass series, the iron has a greater relative impact on the borate sub-network that is partly, but not fully, explained by the work of Wright et al. [19]. The complex tetrahedral avoidance hierarchies suggested by Zhang et al. [132] provide an interesting theory as to why the iron impacts the borate sub-network more than the silicate sub-network in the more complex glass series that includes Al_2O_3, but the effects of the presence of more network modifiers (CaO and Li_2O in the CCFe series, with MgO and SrO added into the HAFe series) cannot be discounted due the documented effects of these modifiers on iron glass, as well as the wider glass network [17,62,104,133]. Further study is needed to fully explore the complex interactions and trtrahedral avoidance hierarchies within these and other oxide glass networks. While the Hanford analogue series glasses were not available for XPS measurements and not suitable for boron K-edge XANES measurements, similar spectroscopic changes to those observed in the SCFe and CCFE series Raman spectra, are observed for the HAFe series Raman spectra. This leads to the view that the borosilicate network in the Hanford analogue glasses will broadly be affected in the same manner as the SCFe and CCFe samples, as evidenced by the same patterns of changes seen in the Raman and RDS spectra. The RDS for the HAFe series in Fig. 18 shows the same changes in the high frequency region as for the SCFe and CCFe RDS in Figs. 20 and 21. The Raman band at approximately 630 cm^{-1} in the HAFe series does not follow the same strict trend in the RDS, with an apparent increase in the band intensity for the HAFe007.1 sample (visible in the stack plot in Fig. 19). The crystalline phase present in samples HAFe007.1 and HAFe010.0 (Fig. 3) is an iron-rich spinel phase with contributions from other transition metals. This is also reflected in the Mössbauer spectra for the two samples in Figs. 6 and 9, with the fitted parameters in Table 7 supporting this phase assignment as a spinel [134,135]. While the low intensity of the peaks in Fig. 3, combined with the low site abundance of the paramagnetic sextet reported in Table 7, would suggest that relative to the amorphous phase, the abundance of the crystalline phase is low. The reported abundance of crystalline phases in the waste glass from which the HAFe series is derived supports this assessment, with reports of as little as a few percent abundance after heat treatment [39,40]. Despite this, the crystalline phase still contains Fe, which removes Fe from the borosilicate network, which in turn will be evidenced by a slight reduction in the effects caused by the increasing Fe content on the borosilicate glass network, which could partly explain the deviation from the trends observed in the Raman spectrum for sample HAFe007.1.

5. Conclusions

This study aimed to elucidate the structural changes in three series of borosilicate glasses relevant to radioactive waste vitrification as a function of varying iron oxide contents using a variety of spectroscopic techniques. ^{57}Fe Mössbauer spectroscopy and Fe *K*-edge XANES were used to show that the iron exists entirely as Fe^{3+}, and predominantly in distorted four-coordinated sites, with some evidence for the presence of low levels of five- and / or six-coordinated sites. This study has qualitatively shown that, in simpler (fewer component) glasses, Fe^{3+} prefers to integrate into the borosilicate network through the silicate subnetwork, evidenced by relative changes in the silicate bands shown in Raman difference spectra; and changes in the XPS Si 2p binding energies relative to the change in B 1 s binding energies (−0.571 eV for the Si 2p, −0.414 for the B 1 s). In contrast, when the glass becomes more complex (more components), Fe^{3+} will integrate more into the glass via the borate subnetwork, as evidenced by relative changes to the borate and borosilicate bands in Raman spectra and an increase in change of XPS B 1 s binding energies when compared to the changes in Si 2p binding energies (−0.447 eV for the Si 2p, −0.570 eV for the B 1 s). These changes occur without significantly affecting the average boron coordination, which was shown to be ~0.45 $^{[4]}B^{3+}$ fraction and ~0.35 $^{[4]}B^{3+}$ fraction for the SCFe and CCFe glass series, respectively. The qualitative evidence gathered by investigating two simpler borosilicate glass compositions was applied to a complex Hanford analogue glass series, HAFe. The similarities in the relative changes in the Raman spectra in terms of the bands associated with silicate and borate units provide evidence that glasses in the HAFe series behave similarly to those in the CCFe series, in that the borate subnetwork is more strongly affected by increasing Fe contents than the silicate subnetwork. This is potentially a consequence of complex FeO_4^- / BO_4^- / AlO_4^- tetrahedral avoidance hierarchies, with the resulting average boron coordination little affected.

CRediT authorship contribution statement

J.D. Eales: Conceptualization, Methodology, Investigation, Formal analysis, Writing – original draft, Writing – review & editing. **A.M.T. Bell:** Resources, Supervision. **D.A. Cutforth:** Resources. **A.A. Kruger:** Supervision, Funding acquisition, Writing – review & editing. **P.A. Bingham:** Conceptualization, Supervision, Funding acquisition, Writing – review & editing.

Declaration of Competing Interest

The authors declare that they have no known competing financial interests or personal relationships that could have appeared to influence the work reported in this paper.

Data availability

Data may be available upon request, subject to securing appropriate approvals

Acknowledgements

The authors acknowledge the Elettra Synchrotron Facility for provision of synchrotron radiation facilities, and we would like to thank Nicola Mahne, Angelo Giglia, and Steffano Nannarone for assistance in using the BEAR beamline. The research leading to this result has been supported by the project CALIPSOplus under grant agreement 730872 from the EU Framework Programme for Research and Innovation HORIZON 2020.

The authors acknowledge the European Synchrotron Radiation Facility for provision of synchrotron radiation facilities, for the allocation of 9 shifts each for the proposals MA-4906 and 28-011280. We would like to thank Paul Thompson and Laurence Bouchenoire for assistance in using beamline XMaS BM28.

The authors also wish to acknowledge the support of the Henry Royce Institute for JDE through the Royce PhD Equipment Access Scheme enabling access to XPS facilities at Royce@Manchester; EPSRC Grant Number EP/R00661X/1. We also wish to thank Dr. Ben Spencer and Dr. Marek Nikiel for assistance in acquiring the XPS data.

The authors would also like to thank the US Department of Energy Office of River Protection and Sheffield Hallam University for the funding of this research.

For the purpose of open access, the author has applied a Creative Commons Attribution (CC BY) licence to any Author Accepted Manuscript version arising from this submission.

Supplementary materials

Supplementary material associated with this article can be found, in the online version, at doi:10.1016/j.jnoncrysol.2023.122664.

References

[1] R.E. Gephart, Hanford – A conversation About Nuclear Waste and Cleanup, Battelle Press, Columbus, Ohio, USA, 2003.
[2] R.A. Peterson, E.C. Buck, J. Chun, R.C. Daniel, D.L. Herting, E.S. Ilton, G. J. Lumetta, S.B. Clark, Review of the scientific understanding of radioactive waste at the U.S. DOE Hanford Site, Environ. Sci. Technol. 52 (2018) 381–396.
[3] S.F. Agnew, J. Boyer, R.A. Corbin, T.A. Duran, J.R. FitzPatrick, K.A. Jurgensen, T. P. Ortiz, B.L. Young, Hanford tank chemical and radionuclide inventories. HDW Model Rev. 4., Los Alamos National Laboratory, 2003. **LA-UR-96-3860**.
[4] J.D. Vienna, Nuclear waste vitrification in the United States: recent developments and future options, Int. J. Appl. Glass Sci. 1 (2010) 309–321.
[5] J.C. Hostetter, H.S. Roberts, Note on the dissociation of ferric oxide dissolved in glass and its relation to the color of iron-bearing glasses, J. Am. Ceram. Soc. 4 (1921) 927–938.
[6] A.K. Lyle, D.E. Sharp, Colour Changes in flint glass, J. Am. Ceram. Soc. 8 (1933) 380–384.
[7] R.L. Shute, A.E. Badger, Effects of iron oxide on melting of glass, J. Am. Ceram. Soc. 25 (1942) 355–357.
[8] B.O. Mysen, F. Seifert, D. Virgo, Structure and redox equilibria of iron-bearing silicate melts, Am. Mineral. 65 (1980) 867–884.
[9] P.A. Bingham, J.M. Parker, T. Searle, J.M. Williams, K. Fyles, Redox and clustering of iron in silicate glasses, J. Non-Cryst. Solid. 253 (1999) 203–209.
[10] H.-I. Kim, J.C. Sur, S.K. Lee, Effect of iron content on the structure and disorder of iron-bearing sodium silicate glasses: a high-resolution ^{29}Si and ^{17}O solid-state NMR study, Geochim. Cosmochim. Acta 173 (2016) 160–180.
[11] M.D. Dyar, A review of Mossbauer data on inorganic glasses: the effects of composition on iron valency and coordination, Am. Mineral. 70 (1985) 304–316.
[12] A. Moguš-Milanković, B. Pivac, K. Furic, D.E. Day, Structural study of iron phosphate glasses, Phys. Chem. Glasses 38 (1997) 74–78.
[13] C.S. Ray, X. Fang, M. Karabulut, G.K. Marasinghe, D.E. Day, Effect of melting temperature and time on iron valence and crystallization of iron phosphate glasses, J. Non-Cryst. Solids 249 (1999) 1–16.
[14] D.E. Day, Z. Wu, C.S. Ray, P. Hrma, Chemically durable iron phosphate glass wasteforms, J. Non-Cryst. Solid. 241 (1998) 1–12.
[15] A.C. Wright, S.J. Clarke, C.K. Howard, P.A. Bingham, S.D. Forder, D. Holland, D. Martlew, H.E. Fischer, The environment of Fe^{2+}/Fe^{3+} cations in a soda-lime-silica glass, Phys. Chem. Glasses: Eur. J. Glass Sci. Technol. B 55 (2014) 243–252.
[16] T.T. Volotinen, J.M. Parker, P.A. Bingham, Concentrations and site partitioning of Fe^{2+} and Fe^{3+} ions in a soda-lime-silica glass obtained by optical absorbance spectroscopy, Phys. Chem. Glasses: Eur. J. Glass Sci. Technol. B 49 (2008) 258–270.
[17] P.A. Bingham, O.M. Hannant, N. Reeves-McLaren, M.C. Stennett, R.J. Hand, Selective behaviour of dilute Fe^{3+} ions in silicate glasses: an Fe K-edge EXAFS and XANES study, J. Non-Cryst. Solids 387 (2014) 47–56.
[18] B. Cochain, D.R. Neuville, G.S. Henderson, C.A. McCammon, O. Pinet, P. Richet, Effects of the iron content and redox state on the structure of sodium borosilicate glasses: a Raman, Mössbauer and boron k-edge XANES spectroscopy study, J. Am. Ceram. Soc. 95 (2012) 962–971.
[19] A.C. Wright, R.N. Sinclair, J.L. Shaw, R. Haworth, P.A. Bingham, S.D. Forder, D. Holland, C.R. Scales, G.J. Cuello, N.M. Vedishcheva, The environment of Fe^{3+}/Fe^{2+} cations in a sodium borosilicate glass, Phys. Chem. Glasses: Eur. J. Glass Sci. Technol. B 58 (2017) 78–91.
[20] A. Ciżman, E. Rysiakiewicz-Pasek, T. Antropova, M. Krupiński, O.A. Pshenko, A. Zarzycki, Effect of the iron content on the structure and electrical properties of sodium borosilicate glasses: XRD, TEM, Mössbauer, FTIR and DIS spectroscopy study, J. Non-Cryst. Solids 531 (2020).
[21] C.M. Jantzen, K.G. Brown, Predicting the spinel-nepheline liquidus for application to nuclear waste glass processing. Part I: primary phase analysis, liquidus measurement, and quasicrystalline approach, J. Am. Ceram. Soc. 90 (2007) 1866–1879.
[22] K.M. Fox, Crystallization in High Level Waste (HLW) Glass Melters: Operational Experience from the Savannah River Site, Savannah River National Laboratory, Aiken, SC, USA, 2014. *SRNL-STI-2013-00724*.
[23] P. Hrma, B.J. Riley, J.V. Crum, J. Matyas, The effect of high-level waste glass composition on spinel liquidus temperature, J. Non-Cryst. Solids 384 (2014) 32–40.
[24] C.M. Jantzen, K.G. Brown, Predicting the spinel-nepheline liquidus for application to nuclear waste glass processing. Part II: quasicrystalline freezing point depression model, J. Am. Ceram. Soc. 90 (2007) 1880–1891.
[25] M. Ahmadzadeh, J. Marcial, J. McCloy, Crystallization of iron-containing sodium aluminosilicate glasses in the $NaAlSiO_4$-$NaFeSiO_4$ join, J. Geophys. Res. Solid Earth 122 (2017) 2504–2524.
[26] A. Deshkar, M. Ahmadzadeh, A. Scrimshire, E. Han, P.A. Bingham, D. Guillen, J. McCloy, A. Goel, Crystallization behavior of iron- and boron-containing nepheline ($Na_2O{\cdot}Al_2O_3{\cdot}2SiO_2$) based model high-level nuclear waste glasses, J. Am. Ceram. Soc. 102 (2018) 1101–1121.
[27] N.J. Cassingham, P.A. Bingham, R.J. Hand, Property modification of a high level nuclear waste borosilicate glass through the addition of Fe_2O_3, *Glass Technol*, Eur. J. Glass Sci. Technol. A 49 (2008) 21–26.
[28] J.C. Cunnane, J.K. Bates, C.R. Bradley, E.C. Buck, W.L. Ebert, X. Feng, J.J. Mazer, D.J. Wronkiewicz, J. Sproull, B.P. McGraill, M.K. Altenhofen, High-Level Waste Borosilicate Glass: A Compendium of Corrosion Characteristics, II, US DoE Office of Waste Management, 1994. Volume.
[29] J.L. Nogues, L.L. Hench, Effect of FeO_3/ZnO on two glass compositions for solidification of Swedish nuclear wastes, Mat. Res. Soc. Symp. Proc. 11 (1982) 273–278.
[30] P. Van Iseghem, W. Timmermans, R. De Batist, Corrosion behavior of TRUW base and reference glasses, Mat. Res. Soc. Symp. Proc. 26 (1984) 527–534.
[31] C.P. Rodriguez, J. Chun, J.V. Crum, N.L. Canfield, E.C.E. Rönnebro, J.D. Vienna, A.A. Kruger, Thermal properties of simulated Hanford waste glasses, J. Am. Ceram. Soc. 100 (2017) 2533–2542.
[32] I.N. Dvorinchenko, S.V. Matsenko, Structure of glasses in the Na_2O–Fe_2O_3–B_2O_3–SiO_2 system, Glass Ceram. 57 (2000) 11–13.
[33] M.F. Taragin, J.C. Eisentein, Mössbauer effect in some complex borosilicate glasses, J. Non-Cryst. Solids 3 (1970) 311–316.
[34] J. Kaewkhao, W. Siriprom, S. Insiripong, T. Ratana, T. Ratana, C. Kedkaew, P. Limsuwan, Structural and magnetic properties of glass doped with iron oxide, J. Phys: Conf. Ser. 266 (2011).
[35] Y.S. Glazkova, S.N. Kalmykov, I.A. Presnyakov, O.I. Stefanovskaya, S. V. Stefanovsky, The structural state of iron in multicomponent aluminum iron borosilicate glass depending on their composition and synthesis conditions, Glass Phys. Chem. 41 (2015) 367–377.
[36] G. El-Damrawi, A.M. Hassan, R. Ramadan, S. El-Jadal, Nuclear magnetic resonance and FTIR structural studies on borosilicate glasses containing iron oxide, New J. Glass Ceram. 6 (2016) 47–56.
[37] M.S. Meikhail, A.M. Abdelghany, Structure and electrical properties of iron borosilicate glasses, Silicon 9 (2017) 895–900.
[38] A. Ratep, I. Kashif, X-ray photoelectron, FTIR, and Mössbauer spectroscopy studied the effect of Fe_2O_3/CuO substitution on structural and electrical properties of lithium borosilicate glasses, J. Mater. Sci.: Mater. Electron. 32 (2021) 12340–12347.

[39] K.S. Matlack, H. Gan, M. Chaudhuri, W.K. Kot, I.L. Pegg, I. Joseph, Melter Throughput Enhancements for High-Iron HLW. *ORP-54002*, Office of River Protection, Richland, WA, USA, 2012.

[40] K.S. Matlack, C. Viragh, W.K. Kot, I.L. Pegg, I. Joseph, Effect of the Form of Iron on HLW Melt Rate. *VSL-15R3430-1*, Vitreous State Laboratory, The Catholic University of America, Washington D.C., USA, 2015.

[41] J. Sułowska, I. Wacławska, M. Szumera, Comparative study of zinc addition effect on thermal properties of silicate and phosphate glasses, J. Therm. Anal. Calorim. 123 (2016) 1091–1098.

[42] H.L. Giles, P.W. Hurley, H.W.M. Webster, Simple approach to the analysis of oxides, silicates and carbonates using x-ray fluorescence spectrometry, X-Ray Spectrom 24 (1995) 205–218.

[43] K. Lagarec, D.G. Rancourt, Recoil – Mössbauer spectral Analysis Software for Windows, Department of Physics, University of Ottawa, Ottawa, ON, Canada, 1998, p. 43, version 1.0, pp.

[44] G. Bunker, An Introduction to EXAFS: A Practical Guide to X-ray Absorption Fine Structure Spectroscopy, Cambridge University Press, Cambridge, UK, 2010.

[45] B. Ravel, M. Newville, ATHENA, ARTEMIS, HEPHAESTUS: data analysis for X-ray absorption spectroscopy using IFEFFIT, J. Synchrotron. Rad. 12 (2005) 537–541.

[46] S. Nannarone, F. Borgatti, A. DeLuisa, B.P. Doyle, G.C. Gazzadi, A. Giglia, P. Finetti, N. Mahne, L. Pasquali, M. Pedio, G. Selvaggi, G. Naletto, M.G. Pelizzo, G. Tondello, The BEAR beamline at Elettra, AIP Conf. Proc. 705 (2004) 450–453.

[47] D.R. Neuville, B.O. Mysen, Role of aluminium in the silicate network: in situ, high-temperature study of glasses and melts on the join SiO_2-$NaAlO_2$, Geochim. Cosmochim. Acta 60 (1996) 1727–1737.

[48] D.A. Long, Raman Spectroscopy, McGraw-Hill Inc., London, UK, 1977.

[49] R. Gautam, S. Vanga, F. Ariese, S. Umapathy, Review of multidimensional data processing approaches for Raman and infrared spectroscopy, EPJ Tech. Instrum. 2 (2015).

[50] D.R. Lide, CRC Handbook of Chemistry and Physics, 88th Edition, CRC Press, Taylor & Francis, Boca Raton, FL, USA, 2007, pp. 2007–2008.

[51] C.K. Kurkjian, E.A. Sigety, Coordination of Fe^{3+} in glass, Phys. Chem. Glass. 9 (1968) 73–83.

[52] C.K. Kurkjian, Mössbauer spectroscopy in inorganic glasses, J. Non-Cryst. Solid. 3 (1970) 157–194.

[53] R.R. Bukrey, P.F. Kenealy, G.B. Beard, H.O. Hooper, Mössbauer-effect study of the structure and magnetic properties of the $Na_2O \cdot Li_2O \cdot B_2O_3 \cdot Fe_2O_3$ glass system, Phys. Rev. B 9 (1974) 1052–1061.

[54] S.S. Sekhon, R. Kamal, Mössbauer study in the glass system $PbO{\cdot}2B_2O_3{\cdot}Fe_2O_3$, J. Non-Cryst. Solid. 28 (1978) 189–192.

[55] T. Nishida, T. Hirai, Y. Takashima, Mössbauer spectroscopic study of nonbridging oxygen atoms in potassium borosilicate glasses, Phys. Chem. Glass. 22 (1981) 94–98.

[56] T. Nishida, A review of structural studies of supersonic conducting borate and semiconducting vanadate glasses by Mössbauer spectroscopy and DTA, J. Non-Cryst. Solids 108 (1989) 87–98.

[57] T. Nishida, Advances in the Mössbauer effect for the structural study of glasses, J. Non-Cryst. Solids 177 (1994) 257–268.

[58] P.A. Bingham, S.D. Forder, R.J. Hand, A. Lavaysierre, Mössbauer studies of phosphate glasses for the immobilisation of toxic and nuclear wastes, Hyperfine Interact 165 (2005) 135–140.

[59] Tomandl, G., Chapter 5, in Glass: Science and Technology, vol. 4B, Ed. Uhlmann, D. R., and Kriedl, N. J., Academic Press, New York, 1990.

[60] A. Ciżman, E. Rysiakiewicz-Pasek, M. Krupiński, M. Konon, T. Antropova, M. Marszałek, The effect of Fe on the structure and electrical conductivity of sodium borosilicate glasses, Phys. Chem. Chem. Phys. 19 (2017) 23318–23324.

[61] S.D. Forder, O.M. Hannant, P.A. Bingham, R.J. Hand, Concerning the use of standards for identifying coordination environments in glasses, J. Phys.: Conf. Ser. 217 (2010).

[62] F. Farges, Y. Lefrère, S. Rossano, A. Berthereau, G. Calas, G.E. Brown Jr., The effect of redox state on the local structural environment of iron in silicate glasses: a combined XAFS spectroscopy, molecular dynamics, and bond valence study, J. Non-Cryst. Solids 344 (2004) 176–188.

[63] M. Wilke, F. Farges, P.-E. Petit, G.E. Brown Jr., F. Martin, Oxidation state and coordination of Fe in minerals: an Fe K-XANES spectroscopic study, Am. Mineral. 86 (2001) 714–730.

[64] W.B. White, M. Matsumura, D.G. Linnehan, T. Furukawa, B.K. Chandrasekhar, Absorption and luminescence of Fe^{3+} of single-crystal orthoclase, Am. Mineral. 71 (1986) 1415–1419.

[65] S.G. Fleet, H.D. Megaw, The crystal structure of yoderite, Acta Crystallogr. 15 (1962) 721–728.

[66] A. Yamamoto, Modulated structure of wustite ($Fe_{1-x}O$) (Three dimensional modulation), Acta Cryst. B 38 (1982) 1451–1456.

[67] F. Farges, Crystal chemistry of iron in natural grandidierites: an X-ray absorption fine-structure spectroscopy study, Phys. Chem. Miner. 28 (2001) 619–629.

[68] A. Feige, P. Ruprecht, A.C. Simon, A.S. Bell, J. Göttlicher, M. Newville, T. Lanzirotti, G. Moore, Calibration of Fe XANES for high-precision determination of Fe oxidation state in glasses: comparison of new and existing results obtained at different synchrotron radiation sources, Am. Mineral. 102 (2017) 369–380.

[69] M. Wilke, G.M. Partzsch, R. Bernhardt, D. Lattard, Determination of the iron oxidation state in basaltic glasses using XANES at the K-edge, Chem. Geol. 220 (2005) 143–161.

[70] G.A. Waychunas, M.J. Apted, G.E. Brown Jr., X-ray K-edge absorption spectra of Fe minerals and model compounds: near-edge structure, Phys. Chem. Miner. 10 (1983) 1–9.

[71] S. Bajt, S.R. Sutton, J.S. Delaney, X-ray microprobe analysis of iron redox states in silicates and oxides using X-ray absorption near edge structure (XANES), Geochim. Cosmochim. Acta 53 (1994) 5209–5214.

[72] L. Galoisy, G. Calas, M.A. Arrio, High-resolution XANES spectra of iron in minerals and glasses: structural information from the pre-edge region, Chem. Geol. 174 (2001) 307–319.

[73] Z. Wu, M. Mosbah-Bonnin, J.P. Duraud, N. Métrich, J.S. Delaney, XANES studies of Fe-bearing glasses, J. Synchrotron Rad. 6 (1999) 344–346.

[74] S. Quartieri, M. Triscari, G. Sabatino, F. Boscherini, A. Sani, Fe and Mn K-edge XANES study of ancient Roman glasses, Eur. J. Mineral. 14 (2002) 749–756.

[75] G. Dalba, N.D. Afify, F. Rocca, X-ray absorption spectroscopy studies of glass structure, Phys. Chem. Glasses: Eur. J. Glass Sci. Technol. B 49 (2008) 149–159.

[76] A. Ceglia, G. Nuyts, W. Meulebroeck, S. Cagno, A. Silvestri, A. Zoleo, K. Nys, K. Janssens, H. Thienpont, H. Terryn, Iron speciation in soda-lime-silica glass: a comparison of XANES and UV-vis-NIR spectroscopy, J. Anal. At. Spectrom. 30 (2015) 1552–1561.

[77] O.L.G. Alderman, M.C. Wilding, A. Tamalonis, S. Sendelbach, S. Heald, C. J. Benmore, C.E. Johnson, J.A. Johnson, H.-Y. Hah, J.K.R. Weber, Iron K-edge X-ray absorption near-edge structure spectroscopy of aerodynamically levitated silicate melts and glasses, Chem. Geol. 453 (2017) 169–185.

[78] A.J. Berry, H.St.C. O'Neill, K.D. Jayasuriya, S.J. Campbell, G.J. Foran, XANES calibrations for the oxidation state of iron in a silicate glass, Am. Mineral. 88 (2003) 967–977.

[79] D.R. Neuville, M.R. Cicconi, C. Le Losq, Ch.13 how to measure the oxidation state of multivalent elements in minerals, glasses, and melts?, in: Magma Redox Geochemistry, Geophysical Monograph, 266, 2021.

[80] H. Okudera, A. Yoshiasa, K.-I. Murai, M. Okube, T. Takeda, S. Kikkawa, Local structure of magnetite and maghemite and chemical shift in Fe K-edge XANES, J. Mineral. Petrol. Sci. 107 (2012) 127–132.

[81] D. Manara, A. Grandjean, D.R. Neuville, Advances in understanding the structure of borosilicate glasses: a Raman spectroscopy study, Am. Mineral. 94 (2009) 777–784.

[82] B.C. Bunker, D.R. Tallant, R.J. Kirkpatrick, G.L. Turner, Multinuclear nuclear magnetic resonance and Raman investigation of sodium borosilicate glass structures, Phys. Chem. Glasses 31 (1990) 31–40.

[83] D.W. Matson, S.K. Sharma, J.A. Philpotts, The structure of high-silica alkali-silicate glasses. A Raman spectroscopic investigation, J. Non-Cryst. Solid. 58 (1983) 323–352.

[84] B.N. Meera, A.K. Sood, N. Chandrabhas, J. Ramakrishna, Raman study of lead borate glasses, J. Non-Cryst. Solid. 126 (1990) 224–230.

[85] B.N. Meera, J. Ramakrishna, Raman spectral studies of borate glasses, J. Non-Cryst. Solid. 159 (1993) 1–21.

[86] W.L. Konijnendijk, J.M. Stevels, The structure of borate glasses studied by Raman scattering, J. Non-Cryst. Solid. 18 (1975) 307–331.

[87] W.L. Konijnendijk, J.M. Stevels, The structure of borosilicate glasses studied by Raman scattering, J. Non-Cryst. Solid. 20 (1976) 193–224.

[88] D. Maniu, I. Ardelean, T. Iliescu, Raman spectroscopic investigations of the structure of $xV_2O_5{\cdot}(1\text{ -x})\ [3B_2O_3 \cdot K_2O]$ glasses, Mater. Lett. 25 (1975) 147–149.

[89] D. Maniu, I. Ardelean, T. Iliescu, S. Cinta, O. Cozar, Raman spectroscopic investigations of the oxide glass system $(1\text{-x})(3B_2O_3.K_2O)xMO$ ($MO=V_2O_5$ or CuO), J. Mol. Struct. 410-411 (1997) 291–294.

[90] T. Iliescu, S. Simon, D. Maniu, I. Ardelean, Raman spectroscopy of oxide glass system $(1\text{-x})[yB_2O_3.zLi_2O].xGd_2O_3$, J. Mol. Struct. 294 (1993) 201–203.

[91] B.O. Mysen, L.W. Finger, D. Virgo, F.A. Seifert, Curve-fitting of Raman spectra of silicate glasses, Am. Mineral. 67 (1982) 686–695.

[92] K. Fukumi, J. Hayakawa, T. Komiyama, Intensity of Raman band in silicate glasses, J. Non-Cryst. Solid. 119 (1990) 297–302.

[93] C. Le Losq, D.R. Neuville, P. Florian, G.S. Henderson, D. Massiot, The role of Al^{3+} on rheology and structural changes in sodium silicate and aluminosilicate glasses and melts, Geochim. Cosmochim. Acta 126 (2014) 495–517.

[94] R. Akagi, N. Ohtori, N. Umesaki, Raman spectra of K_2O–B_2O_3 glasses and melts, J. Non-Cryst. Solid. 293-295 (2001) 471–476.

[95] L. Cormier, D.D.S. Meneses, D.R. Neuville, P. Echegut, In situ evolution of the structure of alkali borate glasses and melts by infrared reflectance and Raman spectroscopies, Phys. Chem. Glasses: Eur. J. Glass Sci. Technol. B 47 (2006) 430–434.

[96] T. Yano, N. Kunimine, S. Shibata, M. Yamane, Structural investigation of sodium borate glasses and melts by Raman spectroscopy. I. Quantitative evaluation of structural units, J. Non-Cryst. Solid. 321 (2003) 137–146.

[97] T. Yano, N. Kunimine, S. Shibata, M. Yamane, Structural investigation of sodium borate glasses and melts by Raman spectroscopy. II. Conversion between BO_4 and BO_2O^- units at high temperature, J. Non-Cryst. Solid. 321 (2003) 147–156.

[98] T. Yano, N. Kunimine, S. Shibata, M. Yamane, Structural investigation of sodium borate glasses and melts by Raman spectroscopy. III. Relation between the rearrangement of super-structures and the properties of glass, J. Non-Cryst. Solid. 321 (2003) 157–168.

[99] G.M. Bancroft, H.W. Nesbitt, G.S. Henderson, C. O'Shaughnessy, A.C. Withers, D. R. Neuville, Lorentzian dominated lineshapes and linewidths for Raman symmetric stretch peaks (800–1200 cm^{-1}) in Q^n (n = 1–3) species of alkali silicate glasses/melts, J. Non-Cryst. Solid. 484 (2018) 72–83.

[100] V. Magnien, D.R. Neuville, L. Cormier, J. Roux, J.-L. Hazemann, O. Pinet, P. Richet, Kinetics of iron redox reactions in silicate liquids: a high-temperature X-ray absorption and Raman spectroscopy study, J. Nucl. Mater. 352 (2006) 190–195.

[101] A.-M. Welsch, J.L. Knipping, H. Behrens, Fe-oxidation state in alkali-trisilicate glasses - A Raman spectroscopic study, J. Non-Cryst. Solid. 471 (2017) 28–38.

[102] C. Le Losq, A.J. Berry, M.A. Kendrick, D.R. Neuville, H.St.C. O'Neill, Determination of the oxidation state of iron in mid-ocean ridge basalt glasses by Raman spectroscopy, Am. Mineral. 104 (2019) 1032–1042.
[103] A.J. Berry, G.A. Stewart, H.St.C. O'Neill, G. Mallmann, J.F.W. Mosselmans, A re-assessment of the oxidation state of iron in MORB glasses, Earth Planet. Sci. Lett. 483 (2018) 114–123.
[104] N. Balasubramanya, Z. Sun, M. Ahmadzadeh, S. Kamali, D.R. Neuville, J., . S.. McCloy, A. Goel, Impact of non-framework cation mixing on the structure and crystallization behavior of model high-level waste glasses, J. Am. Ceram. Soc. 105 (2022) 3967–3985.
[105] J.C. Rigby, D.R. Dixon, D.A. Cutforth, J. Marcial, J. Kloužek, R. Pokorný, A. A. Kruger, A. Scrimshire, A.M.T. Bell, P.A. Bingham, Melting behaviour of simulated radioactive waste as functions of different redox iron-bearing raw materials, J. Nucl. Mater. 569 (2022).
[106] M.E. Fleet, S. Muthupari, Boron K-edge XANES of borate and borosilicate minerals, Am. Mineral. 85 (2000) 1009–1021.
[107] M.E. Fleet, S. Muthupari, Coordination of boron in alkali borosilicate glasses using XANES, J. Non-Cryst. Solid. 255 (1999) 233–241.
[108] H. Sauer, R. Brydson, P.N. Rowley, W. Engel, J.M. Thomas, Determination of coordinations and coordination-specific site occupancies by electron energy-loss spectroscopy: an investigation of boron-oxygen compounds, Ultramicroscopy 49 (1993) 198–209.
[109] L.A.J. Garvie, A.J. Craven, R. Brydson, Parallel electron energy-loss spectroscopy (PEELS) study of B in minerals: the electron energy-loss near-edge structure (ELNES) of the B *K* edge, Am. Mineral. 80 (1995) 1132–1144.
[110] O. Bouty, J.M. Delaye, B. Beuneu, T. Charpentier, Modelling borosilicate glasses of nuclear interest with the help of RMC, WAXS, neutron diffraction and ^{11}B NMR, J. Non-Cryst. Solid. 401 (2014) 27–31.
[111] Y.H. Yun, P.J. Bray, Nuclear magnetic resonance studies of the glasses in the system Na_2O-B_2O_3-SiO_2, J. Non-Cryst. Solid. 27 (1978) 363–380.
[112] Y.H. Yun, S.A. Feller, P.J. Bray, Correction and addendum to " Nuclear magnetic resonance studies of the glasses in the system Na_2O-B_2O_3-SiO_2", J. Non-Cryst. Solid. 33 (1979) 273–277.
[113] W.J. Dell, P.J. Bray, S.Z. Xiao, ^{11}B NMR studies and structural modeling of NaO-B_2O_3-SiO_2 glasses of high soda content, J. Non-Cryst. Solid. 58 (1983) 1–16.
[114] D. Li, G.M. Bancroft, M.E. Fleet, P.C. Hess, Z.F. Yin, Coordination of B in K_2O-SiO_2-B_2O_3-P_2O_5 glasses using B *K*-edge XANES, Am. Mineral. 80 (1995) 873–877.
[115] H. Gan, P.C. Hess, R.J. Kirkpatrick, Phosphorus and boron speciation in K_2O-B_2O_3-SiO_2-P_2O_5 glasses, Geochim. Cosmochim. Acta 58 (1994) 4633–4647.
[116] A.V. Naumkin, A. Kraut-Vass, S.W. Gaarenstroom, C.J. Powell, NIST X-ray Photoelectron Spectroscopy Database: NIST Standard Reference Database 20, 2012. Version 4.1 (web version, https://srdata.nist.gov/xps/.
[117] J.F. Watts, J. Wolstenholme, An Introduction to Surface Analysis by XPS and AES, 2nd Edition, John Wiley & Sons Ltd, Chichester, UK, 2020.
[118] Y. Miura, H. Kusano, T. Nanba, S. Matsumoto, X-ray photoelectron spectroscopy of sodium borosilicate glasses, J. Non-Cryst. Solid. 290 (2001) 1–14.
[119] A. Mekki, D. Holland, C.F. McConville, M. Salim, An XPS study of iron sodium silicate glass surfaces, J. Non-Cryst. Solid. 208 (1996) 267–276.
[120] B.W. Veal, D.J. Lam, A.P. Paulikas, W.Y. Ching, XPS study of CaO in sodium-silicate glass, J. Non-Cryst. Solid. 49 (1982) 309–320.
[121] D. Holland, A. Mekki, I.G. Gee, C.F. McConville, J.A. Johnson, C.E. Johnson, P. Appleyard, M. Thomas, Structure of sodium iron silicate glass - a multi-technique approach, J. Non-Cryst. Solid. 253 (1999) 192–202.
[122] J.E. Stanworth, Oxide glass formation from the melt, J. Am. Ceram. Soc. 54 (1971) 61–63.
[123] W. Gordy, W.J.O. Thomas, Electronegativities of the elements, J. Chem. Phys. 24 (1956) 439–444.
[124] J.C. Slater, Atomic radii in crystals, J. Chem. Phys. 41 (1964) 3199–3204.
[125] J.E. Shelby, An Introduction to Glass Science and Technology, 2nd Edition, Royal Society of Chemistry, Cambridge, UK, 2005.
[126] C.H. Hsieh, H. Jain, A.C. Miller, E.I. Kamitsos, X-ray photoelectron spectroscopy of Al- and B-substituted sodium trisilicate glasses, J. Non-Cryst. Solid. 168 (1994) 247–257.
[127] L. Pauling, The nature of the chemical bond. IV. The energy of single bonds and the relative electronegativity of atoms, J. Am. Chem. Soc. 54 (1932) 3570–3582.
[128] T.A. Clarke, E.N. Rizkalla, X-ray photoelectron spectroscopy of some silicates, Chem. Phys. Lett. 37 (1976) 523–526.
[129] R.K. Brow, C.G. Pantano, Compositionally dependent Si 2p binding energy shifts in silicon oxynitride thin films, J. Am. Ceram. Soc. 69 (1986) 314–316.
[130] R.K. Brow, C.G. Pantano, Hydrolysis reactions at the surface of fluorozirconate glass, J. Am. Ceram. Soc. 71 (1988) 577–581.
[131] L.-S. Du, J.F. Stebbins, Network connectivity in aluminoborosilicate glasses: a high-resolution ^{11}B, ^{27}Al and ^{17}O NMR study, J. Non-Cryst. Solid. 351 (2005) 3508–3520.
[132] Y. Zhang, N. Balasubramanya, N. Stone-Weiss, S. Kamali, R.E. Youngman, P. Florian, A. Goel, Insights into the iron- and phosphorus-induced structural rearrangements in sodium aluminoborosilicate glasses and their impact on melt rheology and crystallization behavior, J. Phys. Chem. C 126 (2022) 21771–21792.
[133] C. Wiegel, L. Cormier, G. Calas, L. Galoisy, D.T. Bowron, Nature and distribution of iron sites in a sodium silicate glass investigated by neutron diffraction and EPSR simulation, J. Non-Cryst. Solid. 354 (2008) 5378–5385.
[134] G.A. Sawatzky, F. van der Woude, A.H. Morrish, Mössbauer study of several ferrimagnetic spinels, Phys. Rev. 187 (1969) 747–757.
[135] S.J. Oh, D.C. Cook, H.E. Townsend, Characterization of iron oxides commonly formed as corrosion products on steel, Hyperfine Interact 112 (1998) 59–66.